LETTER

https://doi.org/10.1038/s41586-019-1261-9

Specialized coding of sensory, motor and cognitive variables in VTA dopamine neurons

Ben Engelhard[1,2], Joel Finkelstein[1,3], Julia Cox[1], Weston Fleming[1], Hee Jae Jang[1], Sharon Ornelas[1], Sue Ann Koay[1], Stephan Y. Thiberge[1,2], Nathaniel D. Daw[1,3], David W. Tank[1,2] & Ilana B. Witten[1,2,3]*

There is increased appreciation that dopamine neurons in the midbrain respond not only to reward[1] and reward-predicting cues[1,2], but also to other variables such as the distance to reward[3], movements[4–9] and behavioural choices[10,11]. An important question is how the responses to these diverse variables are organized across the population of dopamine neurons. Whether individual dopamine neurons multiplex several variables, or whether there are subsets of neurons that are specialized in encoding specific behavioural variables remains unclear. This fundamental question has been difficult to resolve because recordings from large populations of individual dopamine neurons have not been performed in a behavioural task with sufficient complexity to examine these diverse variables simultaneously. Here, to address this gap, we used two-photon calcium imaging through an implanted lens to record the activity of more than 300 dopamine neurons from the ventral tegmental area of the mouse midbrain during a complex decision-making task. As mice navigated in a virtual-reality environment, dopamine neurons encoded an array of sensory, motor and cognitive variables. These responses were functionally clustered, such that subpopulations of neurons transmitted information about a subset of behavioural variables, in addition to encoding reward. These functional clusters were spatially organized, with neighbouring neurons more likely to be part of the same cluster. Together with the topography between dopamine neurons and their projections, this specialization and anatomical organization may aid downstream circuits in correctly interpreting the wide range of signals transmitted by dopamine neurons.

To determine how responses are organized across the population of dopamine (DA) neurons from the mouse ventral tegmental area (VTA), we sought to record at cellular resolution from ensembles of identified DA neurons in a behavioural task with sufficient complexity to engage many of the behavioural variables that are now thought to be of relevance to DA neurons. These variables include reward[1,12], reward-predicting cues[1,2], reward history[11,13], spatial position[3], kinematics (velocity, acceleration and view angle)[4–7] and behavioural choices[10,11,14].

Towards this end, we trained 20 mice on a decision-making task in a virtual-reality environment that encompassed this wide range of behavioural variables ('accumulating towers' task[15]) (Fig. 1a, b; visual snapshots of maze in Extended Data Fig. 1a; Supplementary Video 1). As mice navigated the central stem of the virtual T-maze, they observed transient reward-predicting visual cues on the left and right of the maze stem that signalled which maze arm was most likely to be rewarded (termed the 'cue period') (Fig. 1b; cues consisted of white towers, see Methods). By turning to the side with more cues, the mice received a water reward, whereas turning to the other side resulted in a tone and a 3-s time out. The 2-s period after delivery of the reward or presentation of tone was termed the 'outcome period' (Fig. 1b). As expected, after training, mice tended to turn to the maze arm associated with more cues (Fig. 1c; average percentage correct is $77.6 \pm 0.9\%$ (mean $\pm$ s.e.m.)).

To perform two-photon activity imaging from ensembles of DA neurons during this task, we implanted a gradient index (GRIN) lens above the VTA[16]. Expression of the calcium indicator GCaMP was achieved either by injecting a Cre-dependent GCaMP virus into the VTA of DAT::cre mice, or by crossing a GCaMP reporter line with DAT::cre mice (Fig. 1d, Supplementary Video 2 for sample imaging video; see also Extended Data Fig. 2 for the relationship between spikes and fluorescence in DA neurons). In either case, an mCherry virus was injected into the VTA to facilitate motion correction (Extended Data Fig. 3, see Methods). Using this approach, we recorded the activity of approximately 10–30 DA neurons simultaneously in each of 20 mice during performance of the virtual-reality task (Fig. 1e, f; $n = 303$ DA neurons from 20 mice; 292 neurons were estimated to be in the VTA and 11 in the substantia nigra pars compacta; see Extended Data Fig. 4b for reconstructed locations).

Responses of 284 out of 303 DA neurons were significantly modulated by one or more of the following variables (Fig. 2a): spatial position ($n = 91$, 30%), kinematics ($n = 137$, 45%), reward-predicting cues ($n = 77$, 25%), choice accuracy (whether the trial resulted in reward; $n = 69$, 23%), reward history (whether the previous trial was rewarded; $n = 95$, 31%) and reward ($n = 232$, 77%; significance was assessed based on nested comparisons of the encoding model described below, see Methods). The first five variables were quantified during the cue period, and the final variable (reward) was quantified during the outcome period.

During the cue period, individual neurons exhibited diverse responses to most of these variables (Fig. 2a). For example, neurons that were modulated by spatial position most often exhibited upward ramps, although some displayed downward ramps, consistent with ramps that have previously been identified with fast-scan cyclic voltammetry in the striatum[3,17,18] (example single trials in Extended Data Fig. 1b). Neurons that were selective to kinematics were tuned to a range of velocities, acceleration or view angles. Neurons that responded to reward-predicting cues often, but not always, displayed stronger responses to contralateral versus ipsilateral cues[19]. Neurons that were modulated by accuracy universally displayed higher activity to error (as opposed to correct) trials, whereas neurons that were modulated by previous trial outcome were modulated in either direction.

In contrast to the diverse responses to many of the variables during the cue period (for example, upward versus downward spatial ramps), most neurons responded consistently during the outcome period, with stronger responses to reward than to lack of reward (Fig. 2a).

Thus, for the first time, to our knowledge, we have access to many of the behavioural variables that are thought to be relevant to DA neurons within a single behavioural paradigm. This puts us in a position to achieve our goal of understanding how the responses to these variables are organized across the population of DA neurons. To do this, we need a method to quantify how much of the variance of the neural responses can be attributed to each behavioural variable individually, despite the presence of several behavioural variables.

[1]Princeton Neuroscience Institute, Princeton University, Princeton, NJ, USA. [2]Bezos Center for Neural Circuit Dynamics, Princeton University, Princeton, NJ, USA. [3]Department of Psychology, Princeton University, Princeton, NJ, USA. *e-mail: iwitten@princeton.edu

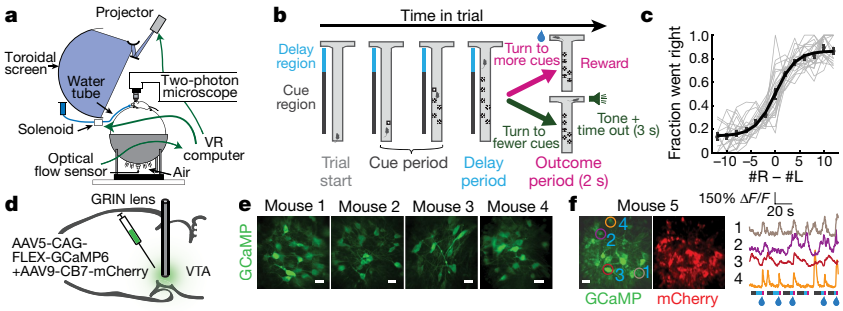

Fig. 1 | Two-photon imaging of VTA DA neuron during navigation and decision-making in virtual reality. a, Schematic of the experimental set-up. VR, virtual reality. **b**, Schematic of an example trial. In the central stem of the maze, the mouse is presented with transient visual cues to either side (cue period). Turning to the arm with more cues results in reward delivery, while turning to the other arm results in a tone and a 3-s time out. **c**, Fraction right choices based on the difference in right versus left cues in each trial. Grey denotes all individual sessions used in this paper; black denotes mean and s.e.m., and the logistic fit to the mean across sessions. **d**, Schematic of the surgical strategy. **e**, Fields of view for four example mice. Scale bars, 20 μm. **f**, Left, simultaneous imaging of GCaMP and mCherry in another example animal, with four neurons demarcated. Right, traces from those four neurons during six consecutive trials. Bars below the traces indicate within-trial epochs: cue period (grey), delay period (blue) and outcome period (pink). Water drops denote reward delivery.

Towards this end, we predicted the GCaMP signal based on the measured behavioural variables with an encoding model (Fig. 2b, Methods). To derive the predictors for the model, each variable was considered as a discrete 'event' variable, a 'whole-trial' variable or a 'continuous' variable. In the case of event variables (left cues, right cues and reward), predictors were generated by convolving the time series of the event with a spline basis set, to allow flexibility in the temporal influence of cues (or reward) on GCaMP. In the case of whole-trial variables (previous reward and accuracy), the value of the binary predictor throughout the trial indicated reward on the previous (or current) trial. In the case of continuous variables (position and kinematics—velocity, acceleration or view angle), predictors included the variables raised to the first, second and third power, to enable flexibility in the relationship between the variable and GCaMP. This model was chosen to include behavioural variables that significantly improved predictions of neural activity, after comparing several models (model comparisons in Extended Data Fig. 1d, e).

Using this encoding model, we quantified the relative contribution of each behavioural variable to the response of each neuron by determining how much the explained variance declined when that variable was removed from the model (see Methods; relative contributions for example neurons are in Extended Data Fig. 5). Averaged across the population, the highest relative contribution during the cue period was attributed to kinematics (32.4 ± 1.9% of the total variance explained during the cue period), followed in descending order by spatial position (22 ± 1.7%), previous reward (17.7 ± 1.5%), cues (14.6 ± 1.4%) and accuracy (13.5 ± 1.5%) (Fig. 2c, d). During the outcome period, reward contributed strongly to the response (74.7 ± 1.8%), consistent with the large number of neurons that responded to reward (Fig. 2a).

Next, we explored how the relative contributions of these behavioural variables to neural responses were distributed across the population. During the cue period, most behavioural variables had a small contribution to the response of each neuron, whereas a small subset had a large contribution. By contrast, during the outcome period, reward contributed to a large fraction of the response of most neurons (Fig. 2d). This raises the possibility that during the cue period, subsets of DA neurons are specialized to encode specific behavioural variables, whereas during the outcome period, most DA neurons encode reward.

To examine this idea more systematically, we performed clustering of the neurons based on the relative contributions of each behavioural variable to each neuron, using a Gaussian mixture model (GMM) (Fig. 3a, Methods). We found that five clusters of neurons gave the best (lowest) Bayesian information criterion (BIC) scores for these data (Fig. 3a; see Methods for details on BIC score calculation). These five clusters explained the data better than expected by chance ($P < 0.0001$, comparing the likelihood of the data given the clustering model to that of shuffled data, for null distributions generated by shuffling across behavioural variables, as well as by shuffling across neurons) (Extended Data Fig. 6a). Thus, we can conclude that VTA DA neurons display a statistically significant degree of functional clustering.

Each cluster was composed of DA neurons that responded most strongly to a specific behavioural variable during the cue period. This specialization does not mean that DA neurons only encoded a single variable during the cue period; in fact, many neurons also significantly encoded a second variable, although not as strongly (Fig. 3b). In contrast to the specialization during the cue period, all clusters were composed of neurons that had reward responses (Fig. 3a, Extended Data Fig. 7a). Thus, this clustering analysis provided further evidence that VTA DA neurons are specialized during the cue period, whereas they share a response to reward during the outcome period. Consistent with the idea that the activity of the cue period differed across clusters, neural activity predicted choice and accuracy to different extents in different clusters (Extended Data Fig. 6b). Supporting the robustness of these clusters, similar cluster assignment was obtained when the procedure was implemented independently on random halves of the trials of each neuron, or with clustering based on a different procedure[20] (Extended Data Fig. 7, see Methods).

We next sought to determine whether the functional clusters of DA neurons were anatomically organized within the VTA. The location of each neuron was estimated based on combining histological reconstruction of the lens tract with the position of the neuron within the imaging field[21] (Extended Data Fig. 4a, b; see Methods). We observed significant dependence of cluster identity on the anteroposterior location for three of the five clusters and on the mediolateral location for four of the five clusters (Fig. 3c, d; $P < 0.01$, comparing the standard deviation of the relative concentration of neurons within a cluster to a shuffled distribution obtained by randomly permuting the anteroposterior or mediolateral location of all neurons relative to cluster identity, Holm–Bonferroni correction; see Methods). Specifically, neurons belonging to the cluster associated with kinematics were located more laterally and posteriorly (cluster 1), neurons associated with accuracy were located more medially and anteriorly (cluster 5), and neurons associated with previous reward were located more laterally (cluster 3).

Directly correlating the anteroposterior and mediolateral location of the neurons with the relative contributions of each behavioural variable led to similar findings (Extended Data Fig. 4c, d). To ascertain that this anatomical organization cannot be explained by differences between individual mice rather than by a true dependence on location, we considered a multinomial mixed effect regression using the cluster identity of the neurons as the dependent variable, the anteroposterior and mediolateral locations as fixed effects, and mouse identity as a random effect for the intercepts. This confirmed that anatomical location

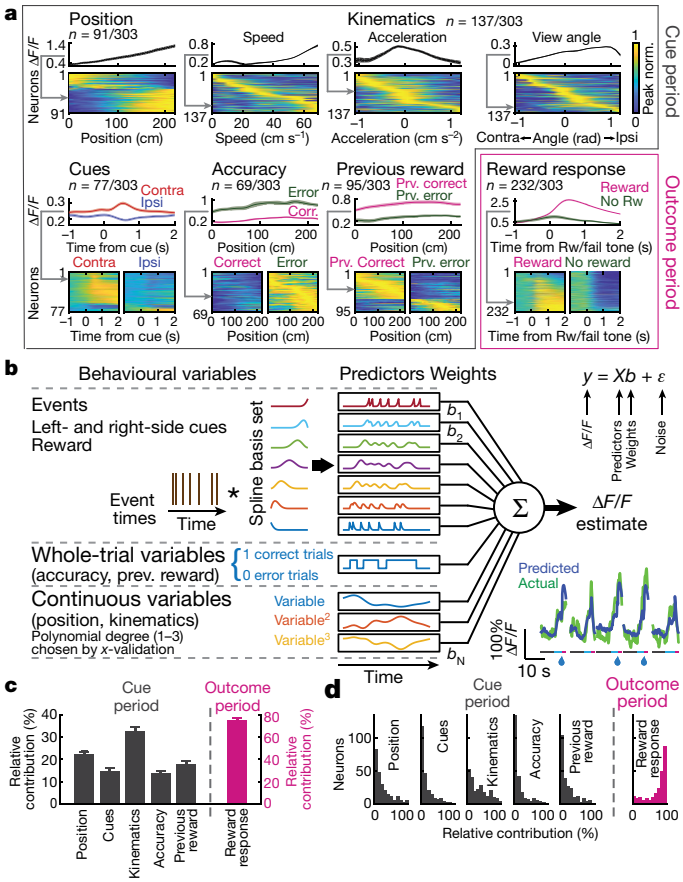

Fig. 2 | Quantification of the responses of VTA DA neurons to specific behavioural variables in the task. a, Neural activity in relation to the following behavioural variables: position along the central stem of the maze, kinematics (speed, acceleration and view angle), cues (contralateral (contra) or ipsilateral (ipsi) to the recording side), accuracy (whether the mouse made the correct choice at the end of the maze), previous trial reward (if the previous trial was rewarded), and reward (Rw) (versus no reward). For each variable, the top panel is the average $\Delta F/F$ signal of an example neuron, and the bottom panel contains all neurons significantly modulated by that variable, with each row representing the peak-normalized average response of each neuron (grey arrow indicates example neuron within heat map). See Methods for statistics and averaging. **b**, Schematic of the encoding model used to quantify the relationship between behavioural variables and the activity of each neuron (see Methods). Inset, predicted and actual $\Delta F/F$ signal across five trials for one neuron; see Extended Data Fig. 1c for additional examples. **c**, Relative contribution of each behavioural variable to the explained variance of the neural activity, averaged across neurons. **d**, As in **c**, but showing the full distribution. All error bars are s.e.m.

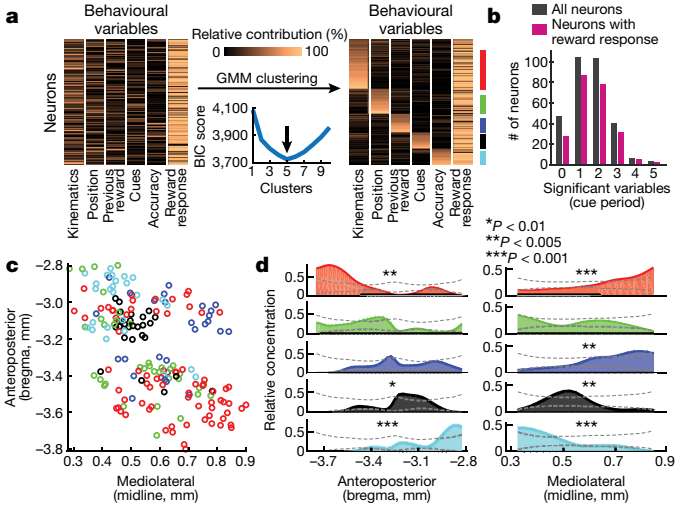

Fig. 3 | Functional and spatial organization of VTA DA neurons. a, The clustering procedure. Left, relative contribution of each behavioural variable to the explained variance of neural activity for each neuron, before clustering (all neurons and variables are shown). Right, the same data grouped based on GMM clustering (ordered within each cluster by the probability of each neuron to belong to the cluster). Coloured vertical lines on the right denote cluster identity (1–5). Neurons with less than 75% probability of belonging to any cluster were not assigned to a cluster (less than 18% of neurons were unassigned). Bottom middle, BIC scores were used to select the optimal number of clusters. **b**, Histogram of the number of behavioural variables during the cue period for which neurons were significantly modulated by. **c**, Recovered locations within the VTA of each neuron along the anteroposterior and mediolateral axes. Colours denote cluster identity. **d**, Relative concentration of neurons belonging to each cluster across the anteroposterior (left) and mediolateral (right) axes. Dashed lines indicate 95% confidence interval (see Methods).

significantly predicted cluster identity ($P < 0.002$, Wald test on the set of null hypotheses that all anteroposterior coefficients in the model are equal to each other, and all mediolateral coefficients are equal to each other; $n = 190$, $\chi^2 = 20.82$, degrees of freedom = 6).

A complementary approach to examine spatial organization in our data is to examine the spatial organization of pairwise correlations between neurons. This allows us to consider separately the spatial organization of the 'signal' correlation (that is, correlations that can be explained by responses to behavioural variables; conceptually related to functional clustering in Fig. 3), and also of the 'noise' correlation (that is, neural correlations that cannot be explained by the behavioural variables). DA neurons are thought to have high noise correlations[22–24], but the spatial organization of these correlations has not been described.

To confirm that DA neurons in our experiment have high noise correlations, we added an additional predictor to the encoding model from Fig. 2b: a 'network' predictor that reflects the activity of other simultaneously imaged neurons (for each neuron, the new predictor was the first principal component of the GCaMP ($\Delta F/F$) signals from all other simultaneously recorded neurons) (Fig. 4a). Consistent with DA neurons having high noise correlations, the performance of this new model explained a substantially higher variance of neural activity (R^2 from behavioural plus network model: 50.7 ± 1%; behaviour-only model: 25.7 ± 0.9%) (Fig. 4b).

We examined the spatial structure of the signal and noise correlations by considering all simultaneously recorded pairs of neurons ($n = 1{,}492$) (Fig. 4c). Signal correlation was defined as the pairwise correlation between the predictions of the behaviour-only encoding model for each neuron; noise correlation was defined as the pairwise correlation between the residuals of the same model. The signal correlation decreased with distance between neurons during the cue period ($\rho = -0.1$, $P < 6 \times 10^{-5}$) but not the outcome period ($\rho = -0.03$, $P < 0.23$). This is consistent with the results from the previous analyses, which had suggested specialized and spatially organized responses during the cue period (Fig. 3d) in contrast to widespread reward responses during the outcome period (Fig. 2a, c). By contrast, noise correlations decreased similarly with distance during both the cue period ($\rho = -0.19$, $P < 4 \times 10^{-13}$) and the outcome period ($\rho = -0.14$, $P < 4 \times 10^{-8}$), which suggests that noise correlations could arise from electrical synapses or shared inputs between neighbouring neurons that are not accounted for in the model. These findings were confirmed using an alternative method for calculating noise correlations[25], and were robust to the level of neuropil correction (Extended Data Fig. 6c, d).

To determine whether the widespread reward responses in VTA DA neurons during the outcome period were consistent with reward prediction error (RPE), we first confirmed that we can replicate the classic RPE during Pavlovian conditioning with two-photon imaging (Fig. 5a–d). We then examined the extent to which reward expectation modulates reward responses in our decision-making task. In this regard, a strength of our task is that it engages two separable

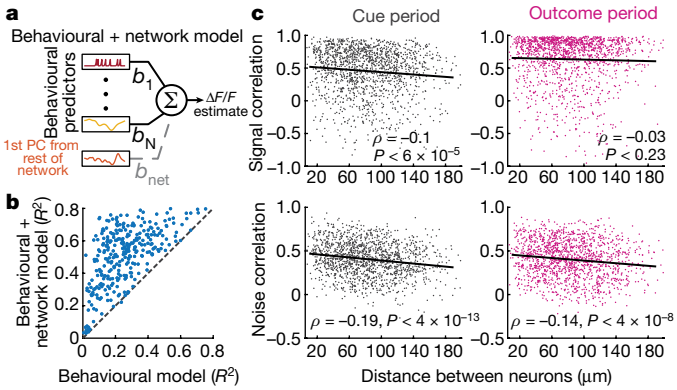

Fig. 4 | Spatial organization of signal and noise correlations in VTA DA neuron pairs. a, Schematic of the expanded encoding model (behavioural plus network model) that includes one additional predictor compared to that in Fig. 2b: the first principal component (PC) of the activity of all simultaneously recorded neurons other than the neuron being modelled. **b**, Comparison of the performance of the behavioural-only and the behavioural plus network models indicates high noise correlations. **c**, Signal and noise correlations for all simultaneously recorded pairs during the cue period (left) and the outcome period (right) as a function of the distance between the neurons ($n = 1{,}492$).

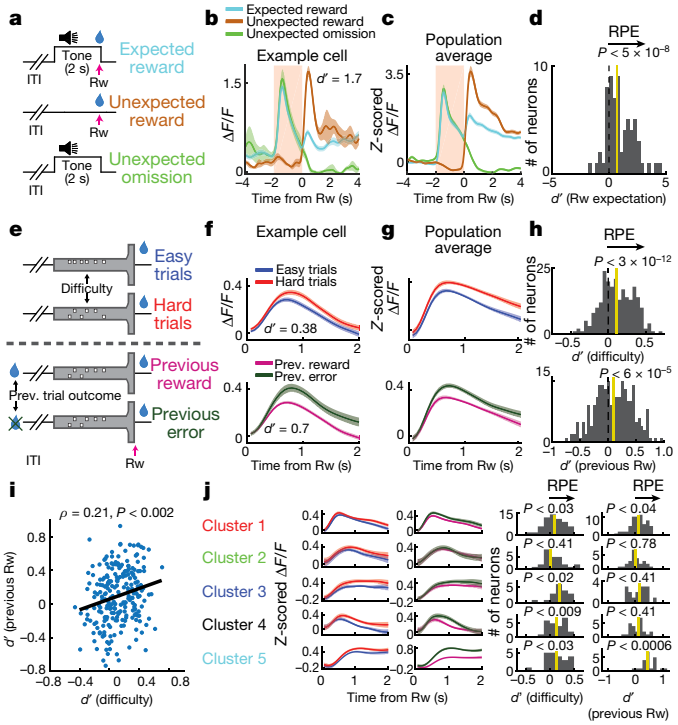

Fig. 5 | Two separable dimensions of reward expectation modulate reward responses in DA neurons during decision-making. a, Schematic of Pavlovian conditioning for data in **b**–**d**. **b**, An example cell in which reward responses are modulated by expectation, consistent with RPE. d' compares the unexpected and expected reward (Rw) response (see Methods). **c**, As in **b**, but the average population response. **d**, Histogram of d' comparisons of unexpected and expected reward for all neurons. $n = 8$ mice and $n = 65$ neurons. **e**, In the virtual-reality T-maze, two dimensions of reward expectation were quantified: trial difficulty and previous trial outcome. Asterisks denote reward delivery. ITI, intertrial interval. **f**, An example DA neuron modulated by both RPE dimensions. **g**, As in **f**, but the average population response. **h**, Histograms of d' comparisons for both RPE dimensions of all reward-responsive neurons ($n = 232$). **i**, Across the population, a significant (but noisy) correlation between the two dimensions of RPE. **j**, Reward responses in most functionally defined clusters (from Fig. 3) are significantly modulated by RPE across at least one dimension, as shown by the average responses (left) and the d' histograms (right; see Methods for details on significance). In all cases, shaded colours are s.e.m.

dimensions of reward expectation: previous trial outcome and trial difficulty (Fig. 5e). If DA neurons reflect RPE, we would expect reward responses to be higher whenever reward expectation is low, for both dimensions of reward expectation (positive d' values; see Methods). Indeed, across the population, reward responses were modulated by expectation in a manner that was consistent with RPE (Fig. 5f–h; median $d' = 0.1$ comparing reward responses based on median splitting trial difficulty, $P < 3 \times 10^{-12}$; median $d' = 0.094$ comparing reward responses across both previous trial outcomes, $P < 6 \times 10^{-5}$; two-sided Wilcoxon signed-rank test and $n = 232$ in both cases). Across neurons, the extent of modulation by each dimension of reward expectation was (weakly) correlated, which suggests that neurons are modulated similarly by each type of RPE (Fig. 5i; $\rho = 0.21$, $P < 0.002$, Pearson correlation between the RPE d' values for previous trial outcome and trial difficulty for all reward responsive neurons, $n = 232$). In addition, reward responses in all but one of the functionally defined clusters are significantly modulated by RPE (Fig. 5j). In further support of the modulation of reward responses by reward expectation, we found that modulation of the reward response depends on task performance in a manner that is consistent with RPE (performance across individuals, Extended Data Fig. 6e; performance during the shaping protocol, Extended Data Figs. 8, 9).

In summary, we have described organizational principles of the DA system: neurons display specialized and anatomically organized responses to non-reward variables, and the same neurons convey a less-specialized reward response. These conclusions depended on combining a high-dimensional behavioural task (6 quantified behavioural variables) with high-dimensional neural recordings (more than 300 identified VTA DA neurons).

Considering the functional and anatomical organization reported here, alongside the established topography between DA neurons and their downstream targets[19,26,27], we can predict that specific downstream targets are likely to receive information from DA neurons about reward and only a subset of non-reward variables. Thus, this organizational structure may greatly simplify the question of how downstream circuits correctly interpret the wide range of non-reward signals encoded by midbrain DA neurons. A major question is how downstream targets use these specialized non-reward signals. One possibility is that these signals reinforce downstream activity patterns related to the encoded variable, altering the probability that the behaviour is repeated (by analogy with the established reinforcement function of reward responses[12,28]). Alternatively, or in addition, they may serve to enhance ongoing activity patterns[29], influencing the vigour of the behaviour[30] but not necessarily the probability of it being repeated in the future. Further experiments will need to be designed to address these hypotheses.

Online content

Any methods, additional references, Nature Research reporting summaries, source data, statements of data availability and associated accession codes are available at https://doi.org/10.1038/s41586-019-1261-9.

Received: 14 May 2018; Accepted: 2 May 2019;
Published online 29 May 2019.

1. Cohen, J. Y., Haesler, S., Vong, L., Lowell, B. B. & Uchida, N. Neuron-type-specific signals for reward and punishment in the ventral tegmental area. *Nature* **482**, 85–88 (2012).
2. Schultz, W., Dayan, P. & Montague, P. R. A neural substrate of prediction and reward. *Science* **275**, 1593–1599 (1997).
3. Howe, M. W., Tierney, P. L., Sandberg, S. G., Phillips, P. E. M. & Graybiel, A. M. Prolonged dopamine signalling in striatum signals proximity and value of distant rewards. *Nature* **500**, 575–579 (2013).
4. Howe, M. W. & Dombeck, D. A. Rapid signalling in distinct dopaminergic axons during locomotion and reward. *Nature* **535**, 505–510 (2016).
5. Barter, J. W. et al. Beyond reward prediction errors: the role of dopamine in movement kinematics. *Front. Integr. Neurosci.* **9**, 39 (2015).

6. Dodson, P. D. et al. Representation of spontaneous movement by dopaminergic neurons is cell-type selective and disrupted in parkinsonism. *Proc. Natl Acad. Sci. USA* **113**, E2180–E2188 (2016).
7. da Silva, J. A., Tecuapetla, F., Paixão, V. & Costa, R. M. Dopamine neuron activity before action initiation gates and invigorates future movements. *Nature* **554**, 244–248 (2018).
8. Coddington, L. T. & Dudman, J. T. The timing of action determines reward prediction signals in identified midbrain dopamine neurons. *Nat. Neurosci.* **21**, 1563–1573 (2018).
9. Kremer, Y., Flakowski, J., Rohner, C. & Lüscher, C. VTA dopamine neurons multiplex external with internal representations of goal-directed action. Preprint at https://www.bioRxiv.org/content/10.1101/408062v1 (2018).
10. Howard, C. D., Li, H., Geddes, C. E. & Jin, X. Dynamic nigrostriatal dopamine biases action selection. *Neuron* **93**, 1436–1450.e8 (2017).
11. Parker, N. F. et al. Reward and choice encoding in terminals of midbrain dopamine neurons depends on striatal target. *Nat. Neurosci.* **19**, 845–854 (2016).
12. Steinberg, E. E. et al. A causal link between prediction errors, dopamine neurons and learning. *Nat. Neurosci.* **16**, 966–973 (2013).
13. Bayer, H. M. & Glimcher, P. W. Midbrain dopamine neurons encode a quantitative reward prediction error signal. *Neuron* **47**, 129–141 (2005).
14. Lak, A., Nomoto, K., Keramati, M., Sakagami, M. & Kepecs, A. Midbrain dopamine neurons signal belief in choice accuracy during a perceptual decision. *Curr. Biol.* **27**, 821–832 (2017).
15. Pinto, L. et al. An accumulation-of-evidence task using visual pulses for mice navigating in virtual reality. *Front. Behav. Neurosci.* **12**, 36 (2018).
16. Barretto, R. P. J., Messerschmidt, B. & Schnitzer, M. J. *In vivo* fluorescence imaging with high-resolution microlenses. *Nat. Methods* **6**, 511–512 (2009).
17. Carelli, R. M. Nucleus accumbens cell firing and rapid dopamine signaling during goal-directed behaviors in rats. *Neuropharmacology* **47** (Suppl. 1), 180–189 (2004).
18. Hamid, A. A. et al. Mesolimbic dopamine signals the value of work. *Nat. Neurosci.* **19**, 117–126 (2016).
19. Kim, H. F., Ghazizadeh, A. & Hikosaka, O. Dopamine neurons encoding long-term memory of object value for habitual behavior. *Cell* **163**, 1165–1175 (2015).
20. Slonim, N., Atwal, G. S., Tkacik, G. & Bialek, W. Information-based clustering. *Proc. Natl Acad. Sci. USA* **102**, 18297–18302 (2005).
21. Cox, J., Pinto, L. & Dan, Y. Calcium imaging of sleep-wake related neuronal activity in the dorsal pons. *Nat. Commun.* **7**, 10763 (2016).
22. Eshel, N., Tian, J., Bukwich, M. & Uchida, N. Dopamine neurons share common response function for reward prediction error. *Nat. Neurosci.* **19**, 479–486 (2016).
23. Joshua, M. et al. Synchronization of midbrain dopaminergic neurons is enhanced by rewarding events. *Neuron* **62**, 695–704 (2009).
24. Kim, Y., Wood, J. & Moghaddam, B. Coordinated activity of ventral tegmental neurons adapts to appetitive and aversive learning. *PLoS ONE* **7**, e29766 (2012).
25. Pillow, J. W. et al. Spatio-temporal correlations and visual signalling in a complete neuronal population. *Nature* **454**, 995–999 (2008).
26. Beier, K. T. et al. Circuit architecture of VTA dopamine neurons revealed by systematic input-output mapping. *Cell* **162**, 622–634 (2015).
27. Lammel, S. et al. Unique properties of mesoprefrontal neurons within a dual mesocorticolimbic dopamine system. *Neuron* **57**, 760–773 (2008).
28. Tsai, H.-C. et al. Phasic firing in dopaminergic neurons is sufficient for behavioral conditioning. *Science* **324**, 1080–1084 (2009).
29. Surmeier, D. J., Ding, J., Day, M., Wang, Z. & Shen, W. D1 and D2 dopamine-receptor modulation of striatal glutamatergic signaling in striatal medium spiny neurons. *Trends Neurosci.* **30**, 228–235 (2007).
30. Panigrahi, B. et al. Dopamine is required for the neural representation and control of movement vigor. *Cell* **162**, 1418–1430 (2015).

Acknowledgements We thank J. Y. Choi, S. S. H. Wang, J. Pillow, D. Witten, L. Pinto, S. Bolkan, D. Lee, N. Engelhard, B. Deverett, A. Song, B. Briones and C. Brody, as well as the BRAINCOGS team, the Bezos Center, the McDonnell Center, and the Witten and Tank laboratories. We also thank E. Engel for reagents. Funding was from ELSC and EMBO (B.E.); NYSCF, Pew, McKnight, NARSAD, and Sloan Foundation (I.B.W.); ARO grants: W911NF-16-1-0474 (N.D.D.), W911NF-17-1-0554 (I.B.W.), and NIH grants U19 NS104648-01, DP2 DA035149-01, 1R01DAA047869-01 and 5R01MH106689-02 (I.B.W.). I.B.W. is a New York Stem Cell Foundation—Robertson Investigator.

Reviewer information *Nature* thanks Regina M. Carelli, Patricia Janak and the other anonymous reviewer(s) for their contribution to the peer review of this work.

Author contributions B.E., D.W.T. and I.B.W. conceived the project. B.E., J.F., J.C., W.F. and S.O. collected data. B.E., W.F., J.C., S.O. and H.J.J. analysed data. S.Y.T. and S.A.K. provided technical training. S.Y.T. built the 2-photon microscope. N.D.D., D.W.T. and I.B.W. advised on the data analysis. B.E. and I.B.W. wrote the paper.

Competing interests The authors declare no competing interests.

Additional information
Extended data is available for this paper at https://doi.org/10.1038/s41586-019-1261-9.
Supplementary information is available for this paper at https://doi.org/10.1038/s41586-019-1261-9.
Reprints and permissions information is available at http://www.nature.com/reprints.
Correspondence and requests for materials should be addressed to I.B.W.
Publisher's note: Springer Nature remains neutral with regard to jurisdictional claims in published maps and institutional affiliations.

METHODS

Animals and surgery. All experimental procedures were conducted in accordance with the National Institutes of Health (NIH) guidelines and were reviewed by the Princeton University Institutional Animal Care and Use Committee (IACUC). A total of 31 mice were used in this study. For the virtual-reality experiments, we used either male DAT::cre mice ($n = 14$, Jackson Laboratory strain 006660; extensively characterized previously[31]) or male mice resulting from the cross of DAT::cre mice and the GCaMP6f reporter line Ai148 mice[32] ($n = 6$, Ai148×DAT::cre, Jackson Laboratory strain 030328; see Extended Data Fig. 10 for validation of co-localization of GCaMP and tyrosine hydroxylase in this line). For the Pavlovian conditioning experiments, we used male and female Ai148×DAT::cre mice ($n = 8$). For the slice recording experiments, we used male and female Ai148×DAT::cre mice ($n = 3$). Mice were maintained on a 12-h light on/12-h light off schedule. All procedures were conducted during their light off period. Mice were 2–6 months old.

Mice between 8–12 weeks underwent sterile stereotaxic surgery under isoflurane anaesthesia (3–4% for induction, 0.75–1.5% for maintenance). The skull was exposed and the periosteum removed using a delicate bone scraper. The edges of the skin were affixed to the skull using a small amount of Vetbond (3M). We injected 800 nl of a viral combination of AAV5-CAG-FLEX-GCaMP6m-WPRE-SV40 ($n = 12$) or AAV5-CAG-FLEX-GCaMP6f-WPRE-SV40 ($n = 2$; University of Pennsylvania Vector Core) with 1.6×10^{12} per ml titre and AAV9-CB7-CI-mCherry-WPRE-rBG (University of Pennsylvania Vector Core) with 2.3×10^{12} per ml titre. Two such injections were made at stereotactic coordinates: 0.5 mm lateral, 2.6 or 3.8 mm posterior, 4.7 mm in depth (relative to bregma). After the injections, we implanted a 0.6-mm diameter GRIN lens (GLP-0673, Inscopix or NEM-060-25-10-920-S-1.5p, GrinTech) in the VTA (coordinates shown in Extended Data Fig. 4) using a 3D-printed custom lens holder. After implantation, a small amount of diluted metabond (Parkell) was applied to affix the lens to the skull using a 1-ml syringe and 18-gauge needle. After 20 min, the lens holder grip on the lens was loosened while the lens was observed through the microscope used for surgery to ascertain there was no movement of the lens. Then, a previously described titanium headplate was positioned over the skull using a custom tool and aligned parallel to the stereotax using an angle meter[33]. The headplate was then affixed to the skull using metabond. A titanium ring to hold the immersion medium was then cemented to the headplate using dental cement blackened with carbon.

Virtual-reality behavioural system. To enable a navigation-based decision-making task under head-fixed conditions, we used a virtual-reality system similar to that previously described[34,35] (Fig. 1a). Mice were held head-fixed under a two-photon microscope using two custom headplate holders and ran on an air-supported, Styrofoam spherical treadmill that was 8 inches (20.3 cm) in diameter. We found that the precise alignment of the mouse on top of the sphere was important for maintaining good behavioural performance; therefore, we used a custom alignment tool for this purpose. The sphere's movement were measured using an optical flow sensor (ADNS3080) located underneath the sphere and controlled by an Arduino Due; this information was sent to the virtual-reality computer, running the ViRMEn software engine[36] (https://pni.princeton.edu/pni-software-tools/virmen) under MATLAB, which displayed and controlled the virtual-reality environment. The measured sphere displacements (dX and dY, in which Y is parallel to the long stem of the T-maze) resulted in translational displacements in the virtual environment of equal length in the corresponding axis. The speed of the mouse was given by $\sqrt{\frac{dX^2}{dt} + \frac{dY^2}{dt}}$, in which d$t$ was the time elapsed from the previous sampling of the sensor. The mouse acceleration was the moment-by-moment change in speed. The mouse view angle in the virtual world was calculated as follows: first, we calculated the current displacement angle as: $\omega = \mathrm{atan2}(-dX \cdot \mathrm{sign}(dY), |dY|)$. Then, the rate of change of the view angle (θ) was given by:

$$\frac{d\theta}{dt} = \mathrm{sign}(\omega)\min\left(e^{(1.4|\omega|^{1.2})} - 1, \frac{\pi}{2}\right) - \theta$$

This exponential function was tuned to stabilize trajectories during the long stem of the maze, while allowing sharp turns into the maze arms (see ref. [15] for more details).

The display was projected using a DLP projector (Mitsubishi HD4000) running at 85 Hz onto a custom toroidal screen with a 270° horizontal field of view. Reward delivery was accomplished by sending by a TTL pulse from the virtual-reality computer to a solenoid valve (NResearch), which released a drop of a water to a lick tube located slightly in front and below the mice's mouth. The tone signifying trial failure was played through conventional computer speakers (Logitech). The setup was enclosed in a custom-designed cabinet built from optical rails (Thorlabs) and lined with sound-absorbing foam sheeting (McMaster-Carr).

Optical imaging and data acquisition. Imaging was performed using a custom-built, virtual-reality-compatible two-photon microscope[35]. The microscope was equipped with a pulsed Ti:sapphire laser (Chameleon Vision, Coherent) tuned to 920 nm. The scanning unit used a 5-mm galvanometer and an 8-kHz resonant scanning mirror (Cambridge Technologies). The collected photons were split into two channels by a dichroic mirror (FF562-Di03, Semrock). The light for the respective green and red channels was filtered using bandpass filters (FF01-520/60 and FF01-607/70, Semrock), and then detected using GaAsP photomultiplier tubes (1077PA-40, Hamamatsu). The signal from the photomultiplier tubes was amplified using a high-speed current amplifier (59-179, Edmund). Black rubber tubing was attached to the objective (Zeiss 20×, 0.5 NA) as a light shield covering the space from the objective to the titanium ring surrounding the GRIN lens. Double-distilled water was used as the immersion medium. The microscope could be rotated along the mediolateral axis of the mice, allowing alignment of the optical axes of the microscope objective and GRIN lens as previously described for microprism imaging[35]. Control of the microscope and image acquisition was performed using the ScanImage software (Vidrio Technologies[37]) that was run on a separate (scanning) computer. Images were acquired at 30 Hz at a resolution of 512 × 512 pixels. Average beam power measured at the front of the objective was 40–60 mW. Synchronization between the behavioural logs and acquired images was achieved by sending behavioural information each time the virtual-reality environment was refreshed from the virtual-reality computer to the scanning computer via an I2C serial bus; behavioural information was then stored in the header of the image files.

Behavioural training. Seven days after the surgery, mice were started on a water restriction protocol, with a daily allotment of water of 1–1.5 ml. Mice were monitored for signs of dehydration or reductions in body mass below 80% of the initial value. If any of these conditions occurred, mice were given ad libitum access to water until recovery. The animals were handled daily from the start of water restriction. Five days after starting water restriction and handling, mice began training in the behavioural setup. Training consisted of a shaping procedure with nine levels of T-mazes with progressively longer stem length and cognitive difficulty (Extended Data Fig. 8). After shaping concluded, in each session the first few trials (5–30) were warm-up trials drawn from mazes 5–8, and then trials from the final maze (#9) were used for the remainder of the session. Warm-up trials were excluded from all analyses presented in the paper. The mice typically received their daily allotment of water during task performance; if not, the remainder was provided to them at the end of the day.

Details of the behavioural task. At the beginning of each trial, mice were presented with the start of a virtual T-maze. After 30 cm (start region) the cue region began, in which cues randomly appeared on either side of the corridor. The number of cues presented was sampled from a Poisson distribution, with means of 6.4 to one of the sides, and 1.3 to the other. To obtain a better estimation of the psychometric curves, we also oversampled easy trials by having 5% of trials with a difference in the number of cues between the sides of 12 or more (using the same probability distributions). The identities of the high-cue-probability and low-cue-probability sides (left or right) were recalculated for each trial to randomize the task and avoid side bias[15]. The locations of the cues were randomly assigned along the cue region using a uniform distribution, with the added constraint of a minimum spatial distance of 14 cm between cues (regardless of their side). Each cue was presented when the mouse arrived 10 cm from its location, and disappeared once it was 4 cm behind the mouse. Thus, the presentation of multiple cues did not overlap in time. The portion of the maze where cues were presented (cue region) was 220 cm long, and after it the stem of the T-maze continued for another 80 cm in which no cues were presented (delay region). At the end of the T-maze, the mouse had to enter one of the arms, and full entry constituted a choice. Turning into the correct (more cues) side would elicit a water reward (6.4 μl), whereas an incorrect choice elicited a tone (pulsing 6–12-kHz tone for 1 s). At the time of reward or tone delivery, the visual environment froze for 1 s, and then disappeared for 2 s (after a successful trial) or 5 s (after a failed trial) before another trial was started.

Pavlovian conditioning. After water restriction and handling, mice were habituated to head fixation for 2–3 sessions. Training consisted of 5 sessions (1 session per day); each session consisted of 50 reward deliveries (8 μl of water reward). During training, each reward was preceded by a 2-s tone that ended at the time of reward delivery. The time between a reward and the next tone delivery was sampled from an exponential distribution with a mean of 40 s. The tone consisted of a sum of multiple sine waves with frequencies of 2, 4, 6, 8 and 16 kHz, and an amplitude of 70 dB. All of the mice exhibited anticipatory licking by the end of the five days (increase in lick rate after tone presentation but before reward delivery). Some of the mice were previously trained for several days in a similar protocol in which the tone amplitude was 60 dB and the time between reward and subsequent tone was sampled from a uniform distribution between 5 and 15 s; these mice did not exhibit anticipatory licking until trained in the final protocol. After training, RPE was assessed in a single test session that consisted of 64 trials; 50 of those trials were identical to the training trials (tone followed by reward), 7 trials were unexpected reward trials (reward delivery with no preceding tone) and 7 trials were unexpected omissions (tone not followed by reward). In all cases, the intertrial

interval was sampled from an exponential distribution with a mean of 40 s. Trial identity was sampled randomly with the following exceptions: (1) the first five trials were standard trials (tone plus reward); (2) the first two non-standard trials were unexpected reward trials.

Session and trial selection. We selected sessions and trials such that each recorded neuron would only appear in one session, and during which mice were engaged in the task. Our dataset contained one main imaging field per mouse, with the exception of three mice, in which we obtained two separate imaging fields at different depths. Thus, we analysed 23 sessions from 20 mice (one session per imaging field). Sessions had at least 100 trials and mice performed at least 65% correct. Mice were between 3 and 6 months old during imaging and were trained for an average of 30 sessions before data collection (a range of 18–51 training sessions).

We removed a small fraction of trials in which mice were not engaged in the task, based on the following criteria: (i) we calculated a smoothed performance measure by processing the binary trials success vector through a zero-phase filter composed of a 21-point-centred Gaussian with standard deviation = 3. Trials in which this measure was less than 0.5 were removed. (ii) A sequence of five or more trials with the same choice and success rate equal to or less than 20% was removed. (iii) A sequence of ten or more trials with the same choice was removed. The removed trials comprised 15% of the trials per session on average. Most of these trials occurred close to the end of the session when the animals tended to exhibit decreased performance. These trials were not removed for consideration of the mice performance when dividing the mice into two groups based on performance, or from the dataset used to divide blocks of trials in a session based on performance (Extended Data Fig. 6). Average performance across sessions on all trials was 73.3 ± 1.1%; average performance after removal of these trials was 77.6 ± 0.9%; average performance on the easiest 20% of trials (based on the absolute difference in cues) after removal was 87% ± 1.7%.

Motion correction procedure. Deep brain imaging can be associated with spatially non-uniform fast motion (frame to frame), as well as spatially non-uniform slow drift of the field of view (over several minutes). To perform accurate motion correction despite the spatial non-uniformity, we divided the video into small regions ('patches') that had relatively uniform motion, and separately corrected the motion within each patch, as described below (schematic of procedure in Extended Data Fig. 3; example video before and after motion correction in Supplementary Video 2). Motion correction was performed on the red channel of the recording when available, otherwise it was performed on the green channel ($n = 9$).

Before dividing the video into patches, we first performed rigid motion correction using a standard normalized cross-correlation method, to eliminate any spatially uniform motion ('matchTemplate' function in the openCV package in Python). This correction was performed on non-overlapping 50-s video clips to eliminate concerns that slow drift over the course of minutes would degrade performance. The template for the cross-correlation was calculated by dividing each clip into non-overlapping sections of 100 frames, calculating the mean image of each section and obtaining the median of the mean images. Before these motion correction steps, the video was pre-processed as follows: (i) thresholded by subtracting a constant number and setting negative values to 0, such that the lower roughly 50% of pixels was 0; (ii) using the openCV function 'erode' (with a scalar '1' kernel); and (iii) convolved with a Gaussian (s.d. = 2 pixels). Motion correction and template calculation were performed iteratively ten times or until all absolute shifts were less than one pixel in both axes. Finally, the 50-s clips had to be aligned to each other. This required generating a 'master template' for the entire video, and then using the same normalized cross-correlation procedure as before ('matchTemplate' function). The master template was calculated by taking the median of the templates of all clips.

The next step of motion correction involved compensating for spatially non-uniform, slow drift by estimating the drift in local patches. Patches were defined manually around neurons of interest to contain objects that drifted coherently (patch width 80–160 pixels). To estimate the drift of each patch over time, we used a non-rigid image registration algorithm (demons algorithm, 'imregdemons' function in MATLAB). This algorithm outputs a pixel-by-pixel correction. However, direct application of this correction risks distorting the shape of the neurons or the amplitude of the signals. Therefore, we applied a uniform correction for each patch, based on the average shift of all pixels in the patch (based on the demons output). We implemented the demons algorithm on the templates from the 50-s clips described in the previous paragraph, again using the median of these templates as the master template. The registration and master templates were computed iteratively 20 times, or until the increase in the average correlation between each corrected template and the overall template was less than the s.e.m. of these correlations. We found that the performance of the non-rigid registration improved if the templates were first processed through a local normalization procedure[38].

Finally, we performed standard rigid motion correction using the normalized cross-correlation method on each patch and clip. We then repeated the rigid motion correction after taking a rolling mean of every two frames and downsampling the video by a factor of two. This increased the signal strength; we used this downsampled video for subsequent analysis. After correcting for motion within clips, we had to correct across clips. To this end, we performed rigid motion correction on the clip templates. The motion correction code can be found in: https://github.com/benengx/Deep-Brain-Motion-Corr.

Calculation of Δ*F*/*F* from the motion-corrected images. The first step in calculating the Δ*F*/*F* for each neuron was to define the region of interest (ROI), as well as the annulus around that ROI that would be used for neuropil correction[39,40]. The ROI of each neuron was defined manually using the mean and s.d. projections of the movie as well as by inspecting a movie that was downsampled by a factor of five. An initial automatic annulus was generated by enlarging the borders of the ROI twice (by 5 μm and 10 μm); the annulus was the shape contained between the two enlarged borders, where we expect that observed activity would be due to the neuropil but not the cell itself. Next, we manually reshaped the annulus region to avoid any visible dendrites, processes or cell bodies, while approximately maintaining its original area.

To correct for neuropil contamination, we subtracted a scaled version of the annulus fluorescence from the raw trace: $F_{corr}(t) = F_{raw}(t) - \Upsilon F_{annulus}(t)$, in which $F_{raw}(t)$ is the mean fluorescence in the ROI of each neuron at time t; $F_{annulus}(t)$ is the mean fluorescence in the corresponding annulus ROI at time t; and Υ is the correction factor[21,39]. The correction factor is intended to reflect the fraction of the z-section that is generated by the neuropil versus the cell that is being imaged. The correction factor used was 0.58, which is consistent with previously reported correction factors in GRIN lens imaging[21,41] and resulted in positive corrected traces. After neuropil subtraction, smoothing was performed by processing the corrected trace through a zero-phase filter using a 25-point centred Gaussian with 1.5 samples points standard deviation.

Δ*F*/*F* at time t was defined as: $(F(t) - F_0(t))/F_0(t)$, in which $F_0(t)$ is the eighth percentile of the smoothed and neuropil-corrected trace based on the preceding 60 s of recording.

Selection of neurons in the dataset. Neurons were selected for analysis based on visual inspection of recording stability, using both the images and the Δ*F*/*F* traces. Only neurons that were stable for at least 50 trials were included in the dataset. The full dataset consisted of 303 neurons from 20 mice. Of these, 233 were considered to have a good fit by the encoding model described in the next section (>5% variance explained by the model during the cue period; reduced dataset). The full dataset was used in Figs. 2a, 3b, 4b, Extended Data Fig. 1. For analyses in which the specific output values of the encoding model were important, we used the reduced dataset composed of neurons for which the encoding model had a good fit (Fig. 2c, d, 3a, c, d, 4c, Extended Data Figs. 4, 6, 7). With regards to the dataset collected throughout learning, neurons that had >5% variance explained by the model during the cue period were used in Extended Data Fig. 8b (except for the 'Model fit' panel, for which all neurons were used). The full learning dataset was used in Extended Data Figs. 8c, 9. When analysing the modulation of outcome activity in rewarded trials (Fig. 5f–j), we used all neurons that had significant reward responses ($n = 232$; see Fig. 2a).

Encoding model. To quantify the contribution of behavioural variables to neural activity, we used an encoding model, which was a multiple linear regression with the Δ*F*/*F* trace of each neuron as the dependent variable, and predictors derived from the behavioural variables as the independent variables (Fig. 2b). To derive the predictors, we divided the behavioural variables into three classes: 'event' variables, 'whole trial' variables and 'continuous' variables. Event variables (left and right cues, and reward) were variables that occurred in discrete points in time. To derive the predictors for these variables, each event was convolved with a 7-degrees-of-freedom regression spline basis set with a 2-s duration, generated using the bs package in R. Whole-trial variables (accuracy and previous reward) were variables in which the value remained constant for an entire trial. These were coded as binary predictors, with a value of '1' in all time points of trials in which the animals received a reward (accuracy) or trials after receiving a reward (previous reward) and '0' elsewhere. Continuous variables (position and kinematics) could change their value at every time point. In the case of kinematics, we included three 'sub-variables' that were closely related to each other: velocity, acceleration and view angle. Up to three predictors were generated per continuous variable (or sub-variable), by raising each variable to the first, second and third powers. The optimal number of predictors to use per continuous variable (for each neuron) was assessed by fivefold cross-validation over trials. We used the position along the maze as a continuous variable rather than the time in trial, based on a previous study[3] that found that on a T-maze in which rats occasionally paused, DA activity seemed to be more closely related to position than time.

The encoding model thus was:

$$F = \beta_0 + \sum_{k=1}^{K_E}\sum_{j=1}^{N_{sp}} \beta_{jk}^{E} e_j^k + \sum_{k=1}^{K_W} \beta_k^{W} w_k + \sum_{k=1}^{K_C}\sum_{j=1}^{d_k} \beta_{jk}^{C} (c_k)^j + \varepsilon$$

in which F is the $\Delta F/F$ signal of a neuron; e_j^k is the jth spline basis function convolved with a binary trace that takes '1' at the times of event occurences and '0' elsewhere, corresponding to the kth event variable; w_k is the predictor for the kth whole-trial variable; c_k is the kth continuous variable; K_E, K_W and K_C are the numbers of event, whole-trial and continuous variables, respectively; N_{sp} is the number of splines (seven in all cases); d_k is the maximal polynomial degree used for each kth continuous variable; the β values are the regression coefficients for the different predictors; and ε is a Gaussian noise term. The β values were calculated using the least squares criterion after z-scoring the predictors (glmfit MATLAB function). The code can be found at https://github.com/benengx/encodingmodel. Example single-trial fits for several cells are shown in Extended Data Fig. 1c.

Model comparison. We tested several behavioural variables to optimize the encoding model. The behavioural variables used in the final model (position, cues, kinematics, accuracy and previous reward) were those the removal of which resulted in a significant degradation of the fit of the model prediction to the data across the population (Extended Data Fig. 1d). Improved fits were assessed by comparing the R^2 for each model (obtained with fivefold cross-validation) using a paired t-test across the population of neurons. We also considered other behavioural variables that did not improve the fit and therefore were not included in the final model (see Extended Data Fig. 1d, e). The other variables that we considered are as follows. Early and late cues: a separate set of predictors was calculated for cues appearing in the first half of the cue region and cues appearing in the second half. $\#L - \#R$: a predictor that at each time point takes the value of the current difference between the number of left-side and right-side cues that had appeared in the trial. $|\#L - \#R|$: a predictor that at each time point takes the absolute value of the current difference between the number of left-side and right-side cues that had appeared in the trial. $\#L$, $\#R$: two predictors that at each time point take the value of the current number of either left-side or right-side cues that had appeared in the trial. P(reward on right) (nominal): a predictor that takes the current probability of the right side being rewarded based on the number of left-side and right-side cues that had appeared in the trial and the sampling statistics of the cues. Given the Poisson distributions from which the cues were sampled (and ignoring the constraint of minimum distance between cues), this probability is given by the following logistic function: $\frac{1}{1+(4.92)^{\#L-\#R}}$, in which $\#L$ and $\#R$ are the current counts of left-side and right-sided cues, respectively. The value of 4.92 is the ratio of Poisson means for high-cue and low-cue probability sides. P(reward) (nominal): a predictor that takes the current probability of being rewarded (that is, making the correct choice) based on the number of left-side and right-side cues that had appeared in the trial and the sampling statistics of the cues. Equivalent to max(P(reward on right),1 − P(reward on right)). P(reward on right) (empirical): a predictor that takes the current probability of the right side being rewarded based on the number of left-side and right-side cues that had appeared in the trial, but instead of using the actual statistics of the cues, this probability was calculated using the psychometric curve of each mouse as the function that related the cue appearances to the probability of each side to be rewarded. Thus, this probability is given by: $\frac{1}{1+a^{\#L-\#R}}$, in which the parameter a is estimated by fitting a logistic function to the psychometric curve of each mouse. P(reward) (empirical): a predictor that takes the current probability of being rewarded (that is, making the correct choice) based on the number of left-side and right-side cues that had appeared in the trial and calculated using the psychometric curve of each mouse as the function that related the cue appearances to the probability of each side to be rewarded. Equivalent to: max(P(reward on right),1 − P(reward on right)). Difficulty of previous trial: a predictor that is the final value of $|\#L - \#R|$ from the previous trial. Confirmatory or disconfirmatory cues: instead of dividing cues in left-sided and right-sided, cues are divided depending on whether they are confirming or disconfirming the current best estimate of the rewarded side. For example, if the current count is three left-sided cues and one right-sided cue, then if the next cue is a left-side cue it is confirmatory, and if it is a right-side cue it is disconfirmatory (in case of an even count the next cue is considered confirmatory).

Calculation of the relative contributions of behavioural variables to neural activity. We quantified the relative contribution of each behavioural variable to neural activity (Figs. 2c, d, 3a, Extended Data Figs. 4c, 5, 6e, f, 7, 8b) by determining how the performance of the encoding model declined when each variable was excluded from the model. We predicted neural activity with all variables (full model) or by excluding one of the variables (partial model), in either case with fivefold cross-validation (over trials; meaning that in each fold 80% of trials were used for training the model and the remainder of trials were used for testing the model performance). The relative contribution of each behavioural variable was calculated by comparing the variance explained of the partial model to the variance explained of the full model. In the case of the cue period, in which there were five behavioural variables, the relative contribution of each variable was defined as $\left(1-\frac{R_{p,i}^2}{R_f^2}\right)/\sum_{j=1}^{5}\left(1-\frac{R_{p,j}^2}{R_f^2}\right)$, in which $R_{p,i}^2$ is the variance explained of the partial model that excludes the ith variable and R_f^2 is that of the full model. In the case of the outcome period, two event variables were considered: time of reward and time of outcome (either reward or tone delivery). The relative contribution of reward was calculated by comparing the variance explained of a partial model with only the time of outcome, compared to a full model that had both time of reward and time of outcome as event predictors, $1-\frac{R_p^2}{R_f^2}$. This allowed us to identify variance in the neural activity that could be attributed to reward rather than simply reaching the end of the maze. Negative relative contributions were set to zero (this occurs when the R^2 of the full model is lower than that of the partial model, owing to introduction of noise by the excluded variable).

We used two approaches to exclude variables from the full model and calculate the variance explained by the partial model. In the first approach, the partial model was equivalent to the full model, except that the β values of the predictors of the excluded variable were set to zero ('no refitting'). In the second approach, we calculated new β values by re-running the regression without the predictors of the excluded variable (refitting). Both approaches to exclude variables produced comparable results; the no-refitting approach was used to generate the main figures, and comparison with the refitting approach is shown in Extended Data Fig. 7b, c, g.

To determine whether the contribution of a behavioural variable was statistically significant for each neuron (Figs. 2a, 3b, Extended Data Figs. 8c, 9), we first calculated the F-statistic of the nested model comparison test in which the reduced model was the model without that behavioural variable included. We then proceeded to calculate the same statistic on 1,000 instances of shuffled data, in which shuffling was performed on non-overlapping 3-s bins (to maintain the autocorrelation of the signal). The P value used for significance was obtained by comparing the value of the original F-statistic to the shuffle distribution, using the Bonferroni correction to account for the number of behavioural variables tested for each neuron; the threshold for significance was a $P = 0.01$ after correction.

To visualize the average responses for all significant neurons for each behavioural variable (Fig. 2a), averaging was performed as follows. In the case of position, accuracy and previous reward, the averaging is over trials. In the case of kinematics, the averaging is over time points. In the case of cues and reward, the averaging was across event occurrences. For the event variables (cues and reward), the average baseline activity was subtracted (in the second preceding the event).

Weighted regression. When calculating the relative contribution of reward (Fig. 2c, d, 3a, Extended Data Figs. 5, 6e, f, 7, 8b) and the decoding performance of choice and accuracy (Extended Data Fig. 6b), we used weighted regression to control for the different number of trials of each type (correct/incorrect trials or left/right choices). Assuming n_a trials of type a and n_b trials of type b, the weights of type a trials are given by: $\frac{n_b}{n_a+n_b}$ and the weights of type b trials are given by: $\frac{n_a}{n_a+n_b}$.

Clustering analysis. To identify functional clusters of neurons (Fig. 3a), we used a clustering procedure based on a GMM that was applied on the matrix of contributions of behavioural variables to the neural activity. To do that, we used the 'fitgmdist' function in MATLAB (Mathworks) with 1,000 maximum iterations, 0.35 regularization value, 100 replicates and the covariance matrix constrained to diagonal. This produces a GMM in which the major axes of the Gaussians are parallel to the axes of the feature space, which enables flexibility beyond that of the k-means algorithm while still maintaining a relatively small number of parameters to be fitted.

To test the fit of the clustering model (Extended Data Fig. 6a), we shuffled 10,000 times the relative contribution values both across behavioural variables (Extended Data Fig. 6a, top) and across neurons (Extended Data Fig. 6a, bottom; the contributions for the cue period variables were re-normalized per neuron after shuffling). After each shuffling iteration, we repeated the clustering and recalculated the log-likelihood of the clustering model. The distribution of log-likelihood values for shuffled data was then compared to the log-likelihood of the clustering model on the real data.

The BIC score was used to select the number of clusters. It is a penalized likelihood term defined as $2(N\log L) + M\log(n)$, in which $N\log L$ is the negative log-likelihood of the data, M is the number of parameters of the GMM and n is the number of observations. The first term rewards model with good fit, whereas the second term penalizes more-complex models. The BIC score was calculated by the 'fitgmdist' function.

Alternative clustering analysis on the predicted traces. In Extended Data Fig. 7i, j, we used an alternative method to cluster the neurons functionally, to compare to the clusters described in Fig. 3. Behavioural predictors from one session were used to generate predicted activity traces based on the encoding model, for each neuron that had more than 5% variance explained by the behavioural model ($n = 233$). A similarity matrix was constructed by taking the absolute correlation between the

predicted traces for each neuronal pair. The similarity matrix was clustered via information-based clustering[20] using the published MATLAB code with parameters: $T = 0.1$, Csize = 5, InitNum = 10. Neurons were assigned a cluster identity to the cluster for which they had the highest probability of belonging, provided that probability was higher than 0.75. The confusion matrix shown in Extended Data Fig. 7j was constructed from neurons that had a cluster identity in both the relative contributions clustering approach (the method used in the main paper) and the alternative method described here (clustering the similarity matrix obtained from the predicted neuronal traces; $n = 158$). The value in bin i, j of the matrix was calculated by: $\frac{\#(\mathrm{ID}_{\mathrm{rel.\ contr.}} = j \wedge \mathrm{ID}_{\mathrm{pred.\ traces}} = i)}{\#(\mathrm{ID}_{\mathrm{rel.\ contr.}} = j \vee \mathrm{ID}_{\mathrm{pred.\ traces}} = i)}$.

Quantification of reward prediction error signals with *d′*. In Fig. 5, the strength of modulation of reward responses by reward expectation was calculated using the d' measure as follows: (1) we divided rewarded trials into trials with either high reward expectation (HRE) or low reward expectation (LRE). For the Pavlovian conditioning experiments, HRE trials were those in which reward delivery was preceded by a tone, and LRE trials were those in which reward delivery was not preceded by a tone. For the virtual-reality experiments, trials were divided in two different ways: for the trial difficulty criterion, we ranked trials according to the strength of the evidence (absolute value of the difference between the total number of right-sided and left-sided cues). The top half of those trials (strong evidence) were considered HRE trials, and the bottom half (weak evidence) were considered LRE trials. For the previous outcome criterion, previously rewarded trials were HRE trials and previously unrewarded trials were LRE trials. (2) We calculated the average reward response in each trial by averaging activity in the first 2 s after reward delivery and subtracting from that the average activity in the 1 s before reward delivery. (3) The d' for the reward responses for HRE and LRE trials was calculated as:

$$d' = \frac{\mu_{\mathrm{LRE}} - \mu_{\mathrm{HRE}}}{\sqrt{0.5(\sigma^2_{\mathrm{LRE}} + \sigma^2_{\mathrm{HRE}})}}$$

in which μ and σ^2 are the mean and variance, respectively, of the distribution of reward responses for the denoted trial group. Thus, positive d' values indicate activity consistent with a reward prediction error signal (stronger reward response for low reward expectation trials). To evaluate whether RPE was significantly represented across the population (Fig. 5d–j), we tested whether the d' distribution was significantly different from zero using a two-sided Wilcoxon signed-rank test. For the d' distributions of the different neuronal clusters (Fig. 5j, right), P values are shown after a Holm–Bonferroni correction for the 10 distributions. The number of neurons assigned to clusters 1 to 5 (which also had a significant reward response) is 62, 26, 18, 25 and 22, respectively.

Histology. After completion of behavioural experiments, mice were deeply anaesthetized with an intraperitoneal injection of euthasol (0.06 ml per 30 g) and transcardially perfused with PBS followed by 4% paraformaldehyde (PFA) in PBS. The brains were then removed and post-fixed in 4% PFA for 24 h before transferring to 30% sucrose in PBS. After post-fixing, 40-μm sections were made with either a microtome (American Optical 860) or a cryostat (Leica CM3050S). Brain sections were washed with PBST (PBS with 0.4% Triton X-100) for 30 min, and then placed in blocking buffer (2% normal donkey serum and 1% bovine serum albumin in 10 ml PBST; Sigma A7906-100G) for 1 h. Sections were incubated overnight at 4 °C in primary antibodies for tyrosine hydroxylase (TH antibody; Aves Labs, E.C. 1.14.16.2, chicken polyclonal anti-peptide antibody mixture, 1:1,000 or 1:200 dilutions) and GFP (Molecular Probes G10362, rabbit monoclonal, 1:1,000 dilution). Sections were then washed with PBST for 30 min, and incubated for 1 h at room temperature in Alexa Fluor 647 (Jackson ImmunoResearch donkey-anti-chicken, 1:1,000 dilution) and donkey anti-rabbit Alexa Fluor 488 (Jackson ImmunoResearch, 711-545-152, 1:1,000 dilution). After PBST washes, sections were mounted in 1:2,500 DAPI in Fluoromount-G (Southern Biotech). Whole sections were imaged with a Nikon Ti2000E microscope or a Hamamatsu NanoZoomer S60.

Estimation of neuron location. To investigate the relationship between the activity of the neurons and their location in the VTA (Fig. 3c, d, Extended Data Fig. 4), we estimated the location of each neuron by combining information about the position of the GRIN lens from histology with the location of the imaged neurons within the field of view. Histological slices stained for tyrosine hydroxylase featuring the tract left by the GRIN lens (Extended Data Fig. 4a) were processed through the Wholebrain software[42] by applying registration points using the VTA, substantia nigra pars compacta and cerebral peduncle as primary markers. The centre of the bottom of the lesion was used as a proxy for the centre of the lens, and its location was provided by the atlas coordinates output of the software. These coordinates are derived from the Allen mouse brain common coordinate framework mapped to stereotactic coordinates[42].

To estimate the optical properties of the GRIN lenses directly, we generated samples from a solution of agarose and fluorescent beads (10 μm, Molecular Probes). We first confirmed the size of the beads by imaging the samples directly with the two-photon microscope that was calibrated by previous imaging of a 10 × 10 μm grid (Thorlabs). We then proceeded to image the samples through the two types of GRIN lenses used. Given that GRIN lenses have different magnifications at different imaging depths, we calibrated the magnification factor at each depth by measuring the observed size of the beads in the x–y axes, and used that size to estimate the magnification factor. To relate the movement of the stage in the z-axis with the imaging depth of the imaged fields, we also measured the observed size of the beads across the z-axis. The z plane used to image each field of view was estimated by identifying the field of view from a z-stack that was previously obtained for each mouse.

For each neuron, the centre of mass of its ROI was used as the marker for the neuron location within the field of view. The absolute location of the neuron was the vector sum of its distance from the lens centre in the field of view to the measured location of the lens centre in atlas coordinates. These estimates were used in Figs. 3, 4 and Extended Data Figs. 4, 6.

The relative concentration across the anteroposterior or mediolateral axes of neurons belonging to a given cluster (Fig. 3d) was calculated as follows. First, the concentration of neurons belonging to a cluster was estimated using Gaussian kernel smoothing via the ksdensity function in MATLAB with a bandwidth of 50 μm applied only on these neurons. Second, the relative concentration for each cluster was calculated as the concentration per cluster divided by the sum of concentrations calculated for all clusters. To calculate the 95% confidence intervals of the relative concentrations (Fig. 3d, dashed lines), we ran 10,000 iterations in which we randomized the cluster identities of the neurons and then proceeded to calculate the relative concentrations of each cluster as above. For each point in the anteroposterior or mediolateral axes, the edges of the confidence interval were the 2.5 and 97.5 percentiles of the distribution of concentrations calculated from the shuffled data. Significant spatial structure for each cluster along each axis was assessed by comparing the standard deviation of the relative concentrations of the data with that obtained from shuffled distributions, in which shuffling was performed 10,000 times by randomizing the locations of the neurons relative to their cluster identity. The obtained P values (Fig. 3d) were then Holm–Bonferroni-corrected for the 10 conditions (5 clusters × 2 axes).

Signal and noise correlations. To investigate how the correlations between pairs of neurons were spatially organized in the VTA, we calculated signal and noise correlations for all pairs of neurons that were simultaneously recorded (Fig. 4c). The signal correlation between a pair of neurons was calculated by correlating the predictions of the encoding model for both neurons in the cue period or outcome period. The noise correlation was the correlation between the residuals for each neuron pair. We also used an alternative method for estimating the noise correlations[25,43] (Extended Data Fig. 6c). The alternative noise correlation estimate between a pair of neurons (i,j) was calculated as follows. We first fit an augmented encoding model for neuron i, which had as an additional predictor the activity of neuron j; we then calculated the normalized improvement in the fit using: $\Delta V_n(i \mid j) = \frac{V(i \mid j) - V(i)}{V(i \mid j)}$, in which $V(i|j)$, $V(i)$ are the variances explained by the augmented and original (behavioural-only) encoding models, respectively, for neuron i. We repeated this procedure for neuron j and obtained $\Delta V_n(j|i)$. The noise correlation estimate was the mean of the two ΔV_n values. To investigate the relationship between pairwise signal and noise correlations and interneuronal distance, we calculated Pearson's linear correlation coefficient and its associated P value between the pairwise correlations and distances for each condition (shown in Fig. 4c, Extended Data Fig. 6c).

Ex vivo recordings to compare GCaMP6f fluorescence with spiking in DA neurons. To compare GCaMP6f fluorescence with spike times in DA neurons (Extended Data Fig. 2), we performed ex vivo slice imaging and electrophysiolgical recordings in Ai148×DAT::cre mice. Mice were deeply anaesthetized with an intraperitoneal injection of euthasol (0.06 ml per 30 g) and decapitated. After extraction, the brain was immersed in ice-cold carbogenated *N*-methyl-D-glucamine (NMDG) artificial cerebrospinal fluid (ACSF) (92 mM NMDG, 2.5 mM KCl, 1.25 mM NaH_2PO_4, 30 mM $NaHCO_3$, 20 mM HEPES, 25 mM glucose, 2 mM thiourea, 5 mM Na-ascorbate, 3 mM Na-pyruvate, 0.5 mM $CaCl_2{\cdot}4H_2O$, 10 mM $MgSO_4{\cdot}7H_2O$ and 12 mM *N*-acetyl-L-cysteine) for 2 min. The pH was adjusted to 7.3–7.4. Afterwards, coronal slices (300 μm) were sectioned using a vibratome (VT1200s, Leica) and then incubated in NMDG ACSF at 34 °C for 15 min. Slices were then transferred into a holding solution of HEPES ACSF (92 mM NaCl, 2.5 mM KCl, 1.25 mM NaH_2PO_4, 30 mM $NaHCO_3$, 20 mM HEPES, 25 mM glucose, 2 mM thiourea, 5 mM Na-ascorbate, 3 mM Na-pyruvate, 2 mM $CaCl_2{\cdot}4H_2O$, 2 mM $MgSO_4{\cdot}7H_2O$ and 12 mM *N*-acetyl-L-cysteine, bubbled at room temperature with 95% O_2, 5% CO_2) for at least 45 min until recordings were performed.

During cell-attached recordings, slices were perfused with a recording ACSF solution (120 mM NaCl, 3.5 mM KCl, 1.25 mM NaH_2PO_4, 26 mM $NaHCO_3$,

1.3 mM $MgCl_2$, 2 mM $CaCl_2$ and 11 mM D-(+)-glucose, continuously bubbled with 95% O_2, 5% CO_2) held at 30 °C. Picrotoxin (100 μM) was added to the recording solution to block tonic inhibition and promote spontaneous activity. Cell-attached recordings were performed using a Multiclamp 700B (Molecular Devices) using pipettes with a resistance of 4–6 MΩ filled with a solution identical to the recording ACSF. Infrared differential interference contrast-enhanced visual guidance was used to select neurons that were 3–4 cell layers below the surface of the slices while the recording solution was delivered to slices via superfusion driven by a peristaltic pump. Cell-attached recordings were collected once a seal (200 MΩ to >5 GΩ) between the recording pipette and the cell membrane was obtained. To generate bursts in cells that did not exhibit spontaneous bursting activity, a second glass pipette filled with recording ACSF containing 20 μM *N*-methyl-D-aspartate (NMDA) was placed above the recorded cell. Slight positive pressure (approximately 80 kPa) was briefly applied (100–250 ms) to generate bursting activity in the recorded cell. During bursts, spikes typically exhibited a gradual reduction in amplitude as previously observed[44]. Action potential currents were recorded in voltage-clamp mode with voltage clamped at 0 mV, which maintained an average holding current of 0 pA. Cell-attached currents were low-pass-filtered at 1 kHz and digitized and stored at 10 kHz (Clampex 9; MDS Analytical Technologies). All experiments were completed within 4 h after slicing the brain. Fluorescence was imaged using a CMOS camera (ORCA-Flash 2.8, Hamamatsu) at 30 Hz using a GFP filter cube set (exciter ET470/40x, dichroic T495LP, emitter ET525/50m).

GCaMP6f kernel estimation. To generate fluorescence traces from simulated spike trains (Extended Data Fig. 7k), we estimated a GCaMP6f kernel[39] using the following equation: $y = e^{-\frac{t}{500}} - e^{-\frac{t}{50}}$, in which $t = [0, 1{,}000]$ (t in ms).

Statistical procedures notes. No statistical methods were used to predetermine sample size. The experiments were not randomized and the investigators were not blinded to allocation during experiments and outcome assessment.

Reporting summary. Further information on research design is available in the Nature Research Reporting Summary linked to this paper.

Code availability

The code for the encoding model and the motion correction is available on github (https://github.com/benengx). All other code is available upon reasonable request.

Data availability

All data are available from the corresponding author upon reasonable request.

31. Lammel, S. et al. Diversity of transgenic mouse models for selective targeting of midbrain dopamine neurons. *Neuron* **85**, 429–438 (2015).
32. Daigle, T. L. et al. A suite of transgenic driver and reporter mouse lines with enhanced brain-cell-type targeting and functionality. *Cell* **174**, 465–480.e22 (2018).
33. Dombeck, D. A., Khabbaz, A. N., Collman, F., Adelman, T. L. & Tank, D. W. Imaging large-scale neural activity with cellular resolution in awake, mobile mice. *Neuron* **56**, 43–57 (2007).
34. Harvey, C. D., Coen, P. & Tank, D. W. Choice-specific sequences in parietal cortex during a virtual-navigation decision task. *Nature* **484**, 62–68 (2012).
35. Low, R. J., Gu, Y. & Tank, D. W. Cellular resolution optical access to brain regions in fissures: imaging medial prefrontal cortex and grid cells in entorhinal cortex. *Proc. Natl Acad. Sci. USA* **111**, 18739–18744 (2014).
36. Aronov, D. & Tank, D. W. Engagement of neural circuits underlying 2D spatial navigation in a rodent virtual reality system. *Neuron* **84**, 442–456 (2014).
37. Pologruto, T. A., Sabatini, B. L. & Svoboda, K. ScanImage: flexible software for operating laser scanning microscopes. *Biomed. Eng. Online* **2**, 13 (2003).
38. Sage, D. & Unser, M. Teaching image-processing programming in Java. *IEEE Signal Process. Mag.* **20**, 43–52 (2003).
39. Chen, T.-W. et al. Ultrasensitive fluorescent proteins for imaging neuronal activity. *Nature* **499**, 295–300 (2013).
40. Kerlin, A. M., Andermann, M. L., Berezovskii, V. K. & Reid, R. C. Broadly tuned response properties of diverse inhibitory neuron subtypes in mouse visual cortex. *Neuron* **67**, 858–871 (2010).
41. Pinto, L. & Dan, Y. Cell-type-specific activity in prefrontal cortex during goal-directed behavior. *Neuron* **87**, 437–450 (2015).
42. Fürth, D. et al. An interactive framework for whole-brain maps at cellular resolution. *Nat. Neurosci.* **21**, 139–149 (2018).
43. Runyan, C. A., Piasini, E., Panzeri, S. & Harvey, C. D. Distinct timescales of population coding across cortex. *Nature* **548**, 92–96 (2017).
44. Mereu, G. et al. Spontaneous bursting activity of dopaminergic neurons in midbrain slices from immature rats: role of *N*-methyl-d-aspartate receptors. *Neuroscience* **77**, 1029–1036 (1997).
45. Lein, E. S. et al. Genome-wide atlas of gene expression in the adult mouse brain. *Nature* **445**, 168–176 (2007).

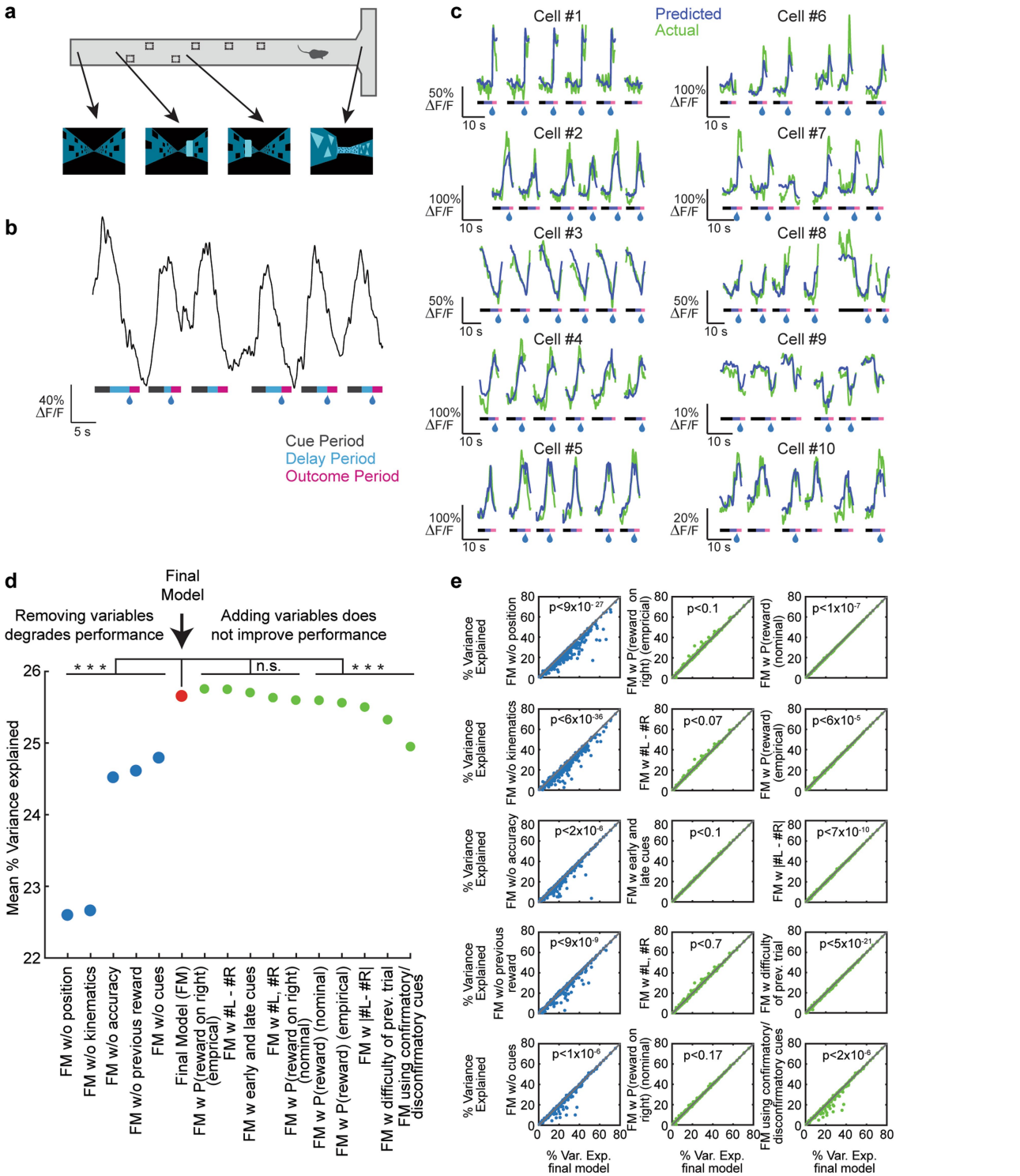

Extended Data Fig. 1 | Features of the virtual-reality task, encoding model predictions and selection of the encoding model. a, Example screenshots of the virtual world presented to the mouse in different positions along the maze. **b**, Activity trace during six consecutive trials of an example neuron that was significantly modulated by position in the central stem ($P = 0$, statistical significance was assessed by comparing the F-statistic obtained from a nested model comparison with or without position to a distribution of the same F-statistic obtained from shuffled data; see Methods). The coloured strip below the trace describes the trial epochs. Reward delivery is denoted by a water droplet. **c**, $\Delta F/F$ traces for ten example neurons during six consecutive trials (green). Overlaid are the predictions of the behavioural model for these trials (blue). The coloured strip below each trace denotes the trial epochs. Reward delivery is denoted by a water droplet. **d**, Mean (across neurons) of percentage variance explained (tested on held-out data with fivefold cross-validation) by the final model (red) and other models in which variables was either removed (blue) or added (green). See Methods for descriptions of all variables tested. All models for which a variable was removed from the final model performed significantly worse, based on comparing R^2 for all neurons ($P < 2 \times 10^{-6}$, two-sided paired t-test, $n = 303$, Holm–Bonferroni correction for all model comparisons). For models in which variables were added to those in the final model, the performance either did not exhibit a significant difference, or was degraded. See Methods for complete description of all models. **e**, Comparison of performance for all neurons of the final model (x axis) and all the other models. Each panel shows the comparison with one model; significance of the two-sided paired t-test (after Holm–Bonferroni correction) is shown in each panel. $n = 303$ in all cases.

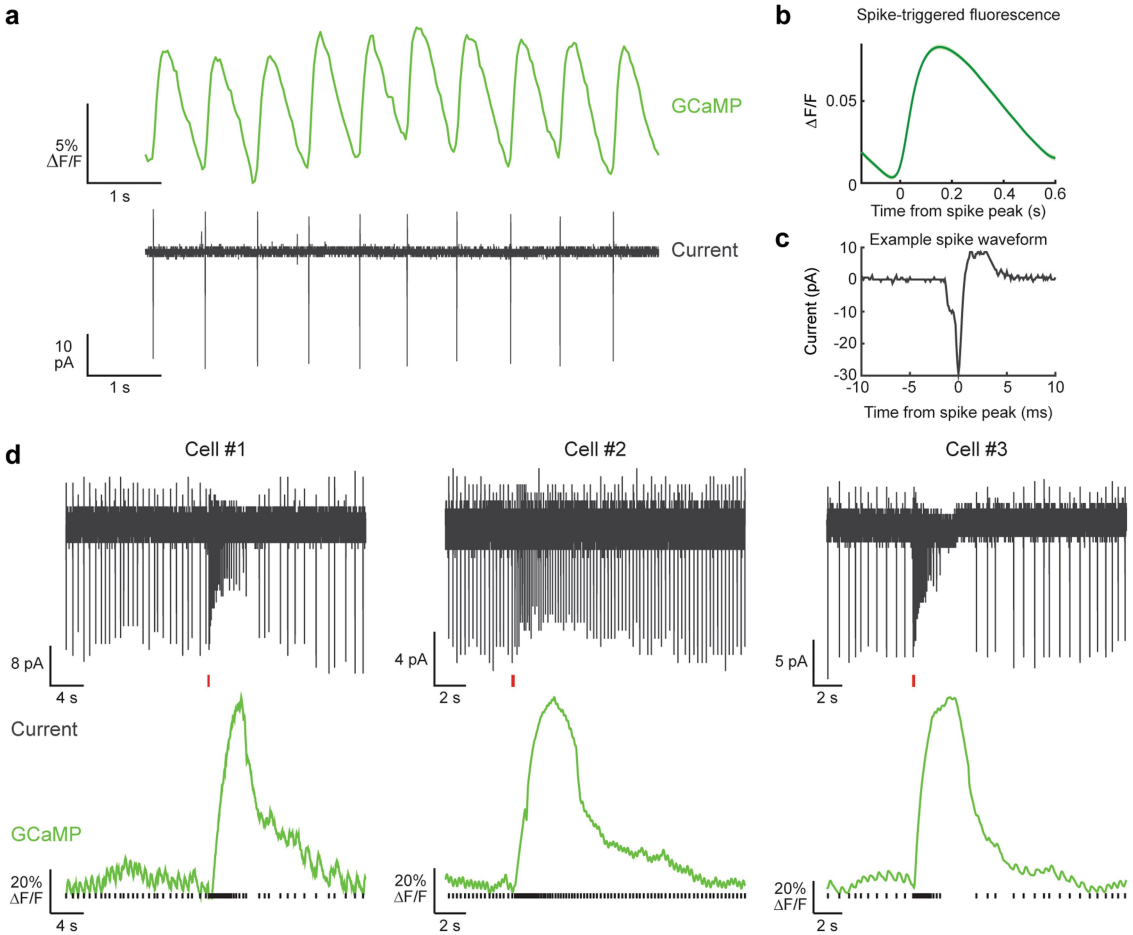

Extended Data Fig. 2 | Simultaneous calcium imaging and cell-attached recording in DA neurons in the VTA of Ai148×DAT::cre mice. a, Relative change in fluorescence (top) and cell-attached current (bottom) recorded simultaneously. **b**, Average spike-triggered fluorescence (averaged over $n = 126$ spikes) for the cell in **a**. **c**, Magnified spike waveform for cell in **a**. **d**, Examples of bursts from three different DA cells, showing cell-attached current (top) and change in fluorescence (bottom). The spike times are shown with black bars under the fluorescence trace. The red horizontal bars under the current traces show the timing of NMDA puffs (see Methods).

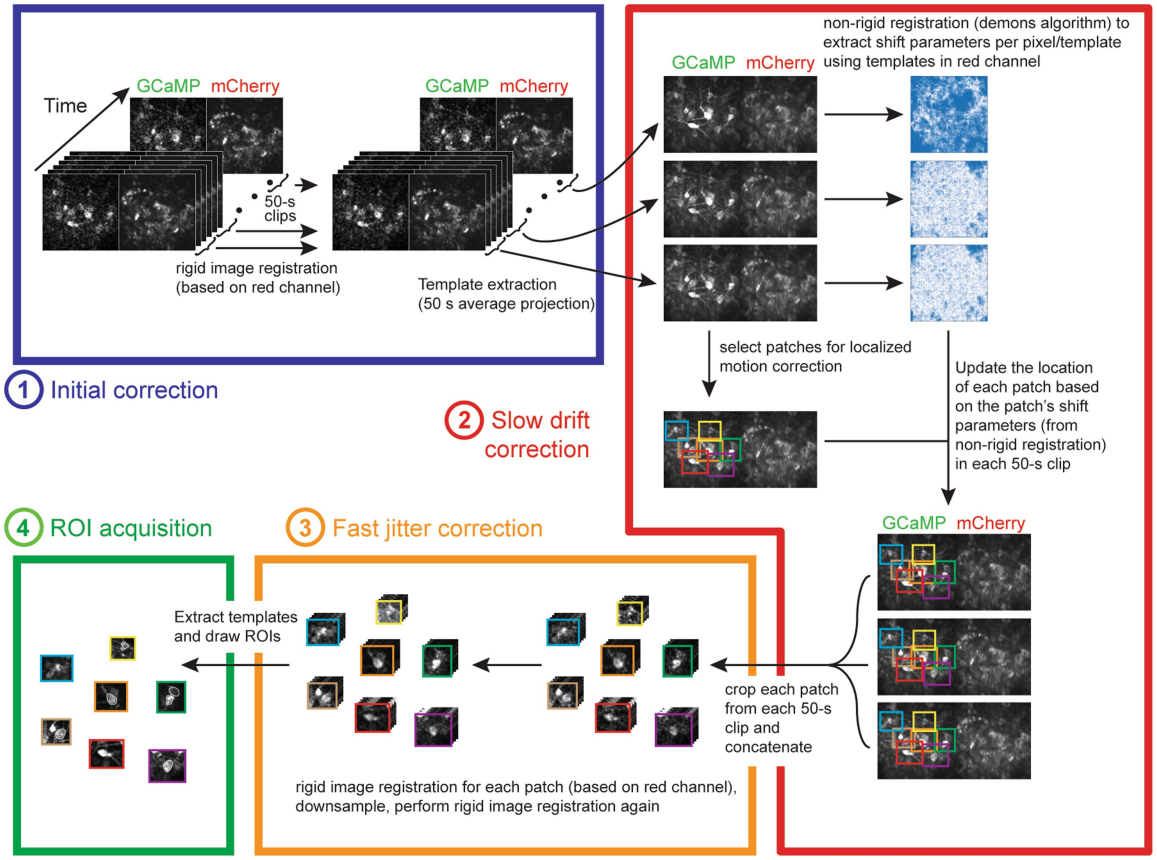

Extended Data Fig. 3 | Motion-correction procedure. We developed a custom motion-correction procedure to compensate for both non-rigid slow drift of the field of view (timescale of tens of minutes) as well as non-rigid fast motion (timescale of tens of milliseconds). Importantly, the procedure avoids any use of interpolation, which can produce artefacts. The procedure consists of the following main steps. (1) Blue box. The entire movie is divided in non-overlapping 50-s clips; in each clip we perform rigid motion correction using standard cross-correlation methods (on the red channel). The template for each clip is calculated by dividing the clip into non-overlapping sections of 100 frames, calculating the mean image of each section, and obtaining the median of the mean images. (2) Red box. We use a non-rigid algorithm for image registration to align all the templates. The algorithm outputs shift parameters for every pixel and template. Separately, we manually draw patches that include neurons of interest in the first template. For each template, we use the shift parameters of all the pixels in each patch to estimate the average motion of the patch. We use that information to crop the patch from each 50-s clip of the movie. (3) Orange box. We perform rigid motion correction (as above) on the concatenated patch movies, down-sample by a factor of two (to increase the signal strength) and then perform rigid motion correction again. (4) Green box. We extract the patch templates by using the mean projection, and hand-draw ROIs of the neurons. See Methods for a detailed explanation of the motion-correction algorithm, and Supplementary Video 2 for an example video before and after correction. Code is available at https://github.com/benengx/Deep-Brain-Motion-Corr.

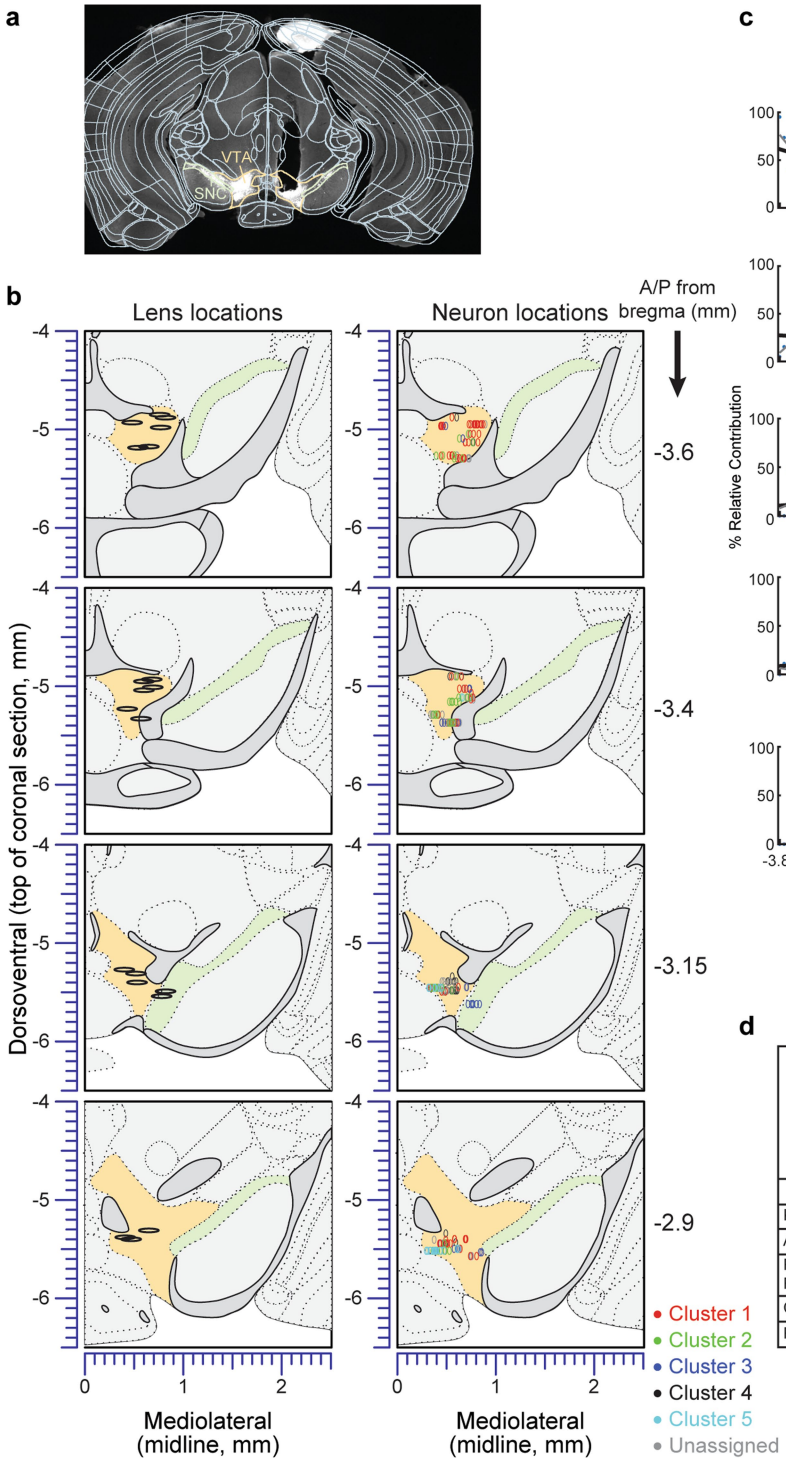

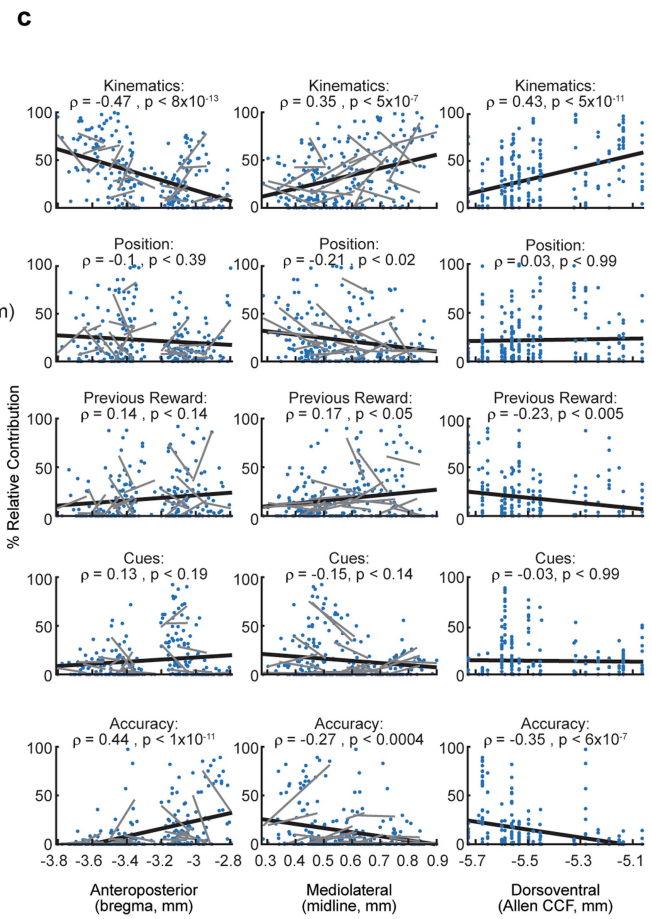

d

	p-values of mixed effect model to predict the relative contribution of each variable for each neuron based on M/L, A/P, D/V (plus pairwise interactions).		p-values of linear regression to predict the average relative contribution for each FOV based on M/L, A/P, D/V (plus pairwise interactions).		p-values of linear regression to predict the average relative contribution for each FOV based on M/L, A/P, D/V (plus pairwise interactions; weighted by # of neurons/FOV).	
	p-value	F-stat.	p-value	F-stat.	p-value	F-stat.
Kinematics	0.00289	3.43539	0.00799	5.11164	0.00548	5.62717
Accuracy	0.00553	3.14756	0.05849	2.84012	0.01282	4.50933
Previous Reward	3.64×10^{-5}	5.33072	0.00028	11.0237	0.00039	10.2541
Cues	0.54809	0.82956	0.68713	0.65443	0.79772	0.49886
Position	0.15729	1.56862	0.18137	1.80213	0.13294	2.07397

Extended Data Fig. 4 | See next page for caption.

Extended Data Fig. 4 | Recovered neuron locations and validation of the spatial organization of neural responses. a, Example of lens location recovery. Coronal histological slices stained for tyrosine hydroxylase were aligned to the Allen Brain Atlas[45] using the Wholebrain software package[42]. The centre of the lens was marked and its position in common coordinates was recovered using the software. SNC, substantia nigra pars compacta. **b**, Left, recovered centres of GRIN lenses from all mice (black ellipses) are shown on top of the atlas images. Right, recovered locations of all neurons that entered the clustering analysis based on an encoding model R^2 during the cue period >5% ($n = 233$; see Methods for details of location recovery). Neurons are colour-coded according to their cluster identity. A/P, anteroposterior. **c**, Relative contributions of each behavioural variable as a function of neuron location along the anteroposterior, mediolateral and dorsoventral axes. In each row, the relative contribution of a behavioural variable is correlated with the anteroposterior (left), mediolateral (middle) or dorsoventral (right) locations. The correlation value and significance (after Holm–Bonferroni correction for all tests) is shown in the panel ($n = 233$ in all cases). The linear fit of the entire population is shown by a black line, and linear fits of neurons belonging to individual mice (which had more than five neurons) are shown by grey lines. **d**, Statistical tests of the spatial organization of responses to different behavioural variables that account for individual differences across mice. The table lists the *P* values and *F*-statistics obtained for three statistical tests for the spatial organization of the cue-period variables. The first test was a mixed effect model that included all neurons that had good fit to the behavioural model during the cue period ($R^2 > 5\%$, $n = 233$). In this model, the relative contribution for a given variable to each neuron was the dependent variable; the anteroposterior, mediolateral and dorsoventral locations and their pairwise interactions were independent fixed effects; and the mouse identity was a random effect for the intercepts (MATLAB code: model = fitglme(Data,'variable~ml∗ap∗dv-ml:ap:dv+(1|mouseID)')). For this test, the degrees of freedom for the numerator and denominator were 6 and 226, respectively. In the field of view (FOV) tests, for every variable we averaged the relative contributions of all neurons in a given FOV (for mice that had two FOVs, we combined neurons from the two FOVs). A regression was run with the average relative contributions as the dependent variable, and the anteroposterior, mediolateral and dorsoventral lens' locations and their pairwise interactions were independent fixed effects ($n = 19$). In the weighted version of the FOV test, we also weighed each FOV observation by the number of neurons in that FOV. For these two tests, the degrees of freedom for the numerator and denominator were 6 and 12, respectively. In all cases, the listed *P* values correspond to the *F*-test for the fixed effects. M/L, mediolateral. D/V, dorsoventral.

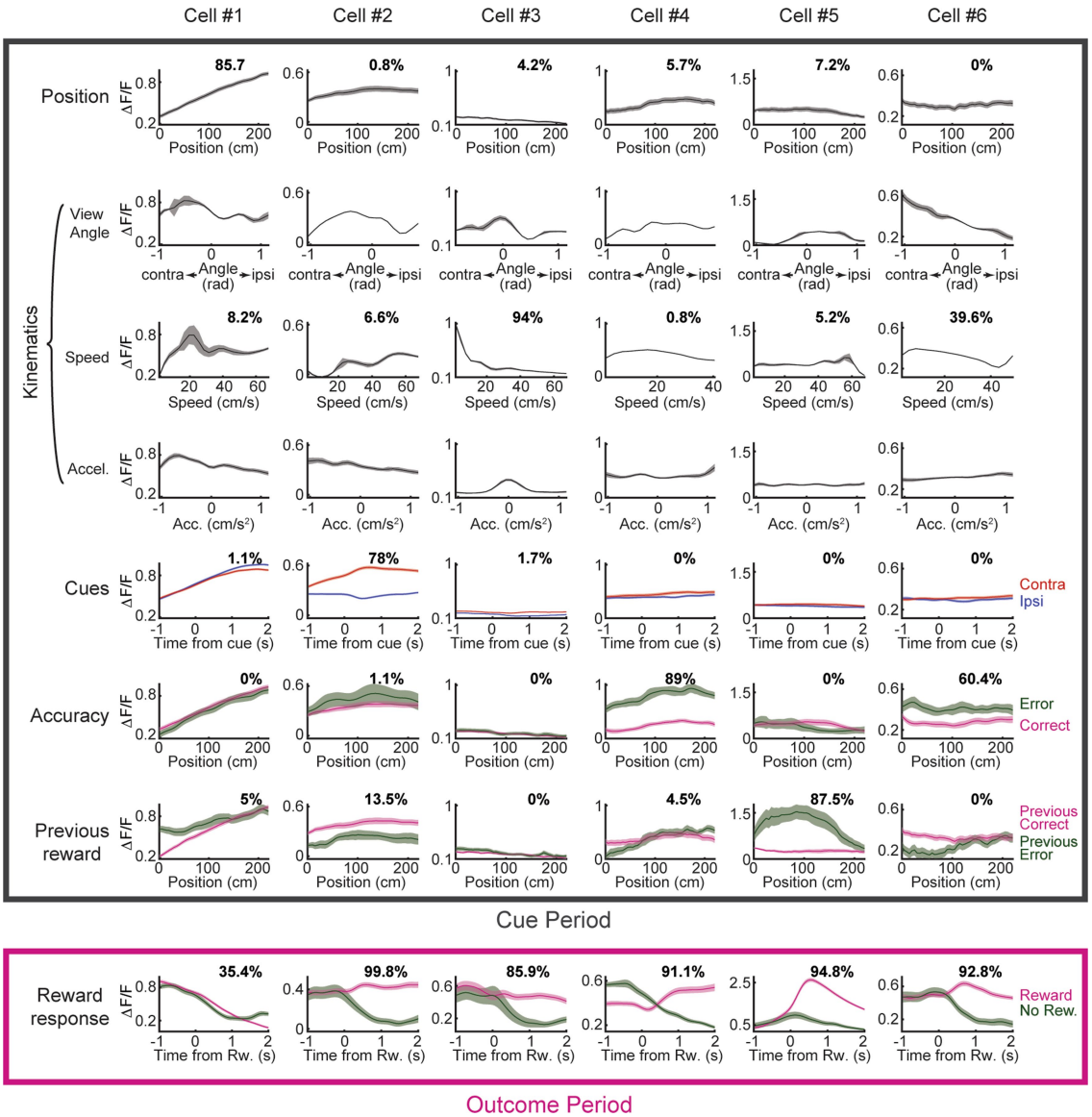

Extended Data Fig. 5 | Average activity and relative contributions of different behavioural variables for several example cells. The panels show activity averages time-locked to different behavioural variables for six example cells. The percentage of relative contribution of the corresponding behavioural variable to the activity of each cell is shown.

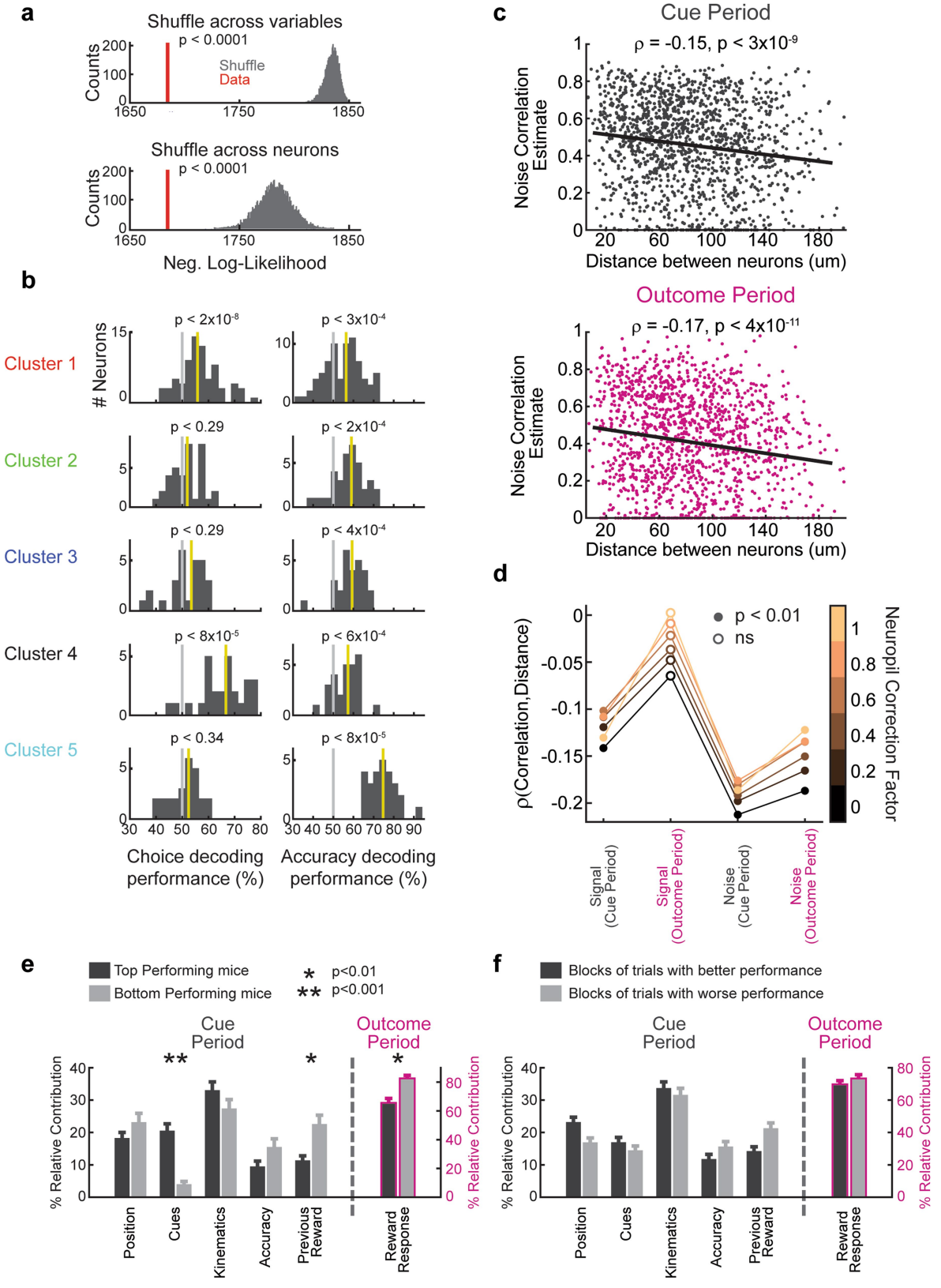

Extended Data Fig. 6 | See next page for caption.

Extended Data Fig. 6 | Additional analyses of neural encoding. **a**, Distributions of the negative log-likelihood of the clustering model (Fig. 3) for shuffled (grey) versus real (red) data indicates a significant fit of the clustering model. Shuffling of relative contributions across variables (top) and across neurons (bottom). **b**, Prediction of choice and accuracy from neurons in each cluster. For each neuron, decoding was performed by logistic regression using the average cue period activity (on a trial-by-trial basis) to predict choice or accuracy. Regression was performed using tenfold cross-validation (over trials). Separate decoders were trained to predict either choice or accuracy. Weighted decoding was used to control for the different number of trials of each type (left/right choices or correct/incorrect trials; see Methods). Each panel shows a histogram of the decoding performance for a given variable (left column: choice, right column: accuracy) and a given cluster (rows). Grey vertical lines indicate 50% performance (chance level). Vertical yellow lines indicate the median of the distribution. Significance was assessed by a two-sided Wilcoxon signed-rank test after a Holm–Bonferroni correction for the ten tests. For clusters 1 to 5, $n = 74$, 36, 27, 27 and 26, respectively. The predictive power of the different clusters is broadly consistent with their association with the different behavioural variables: choice was significantly predicted by neurons belonging to clusters 1 (associated primarily with kinematics, which contains view angle) and 3 (associated primarily with cues, which determine choice for successful trials). The strongest predictive power for the mice's accuracy is exhibited by cluster 5, which is primarily associated with accuracy. **c**, Noise correlations estimated by an alternative method. Here, noise correlations were estimated by calculating the increase in variance explained by the behavioural-only encoding model when the second neuron's activity was added to it as a predictor[25,43]. The noise correlation estimate is shown for all neuronal pairs ($n = 1{,}492$) during the cue period (left) and outcome period (right). **d**, To investigate the possible effect of neuropil contamination on the observed relationship between pairwise correlations and distance (Fig. 4), we recalculated the relationship between correlations and interneuronal distance as a function of the neuropil correction factor. In all cases, we find a similar pattern to that presented in Fig. 4. **e**, To investigate the relationship between task performance and neural encoding, mice were divided into two groups based on their task performance. The relative contributions of the behavioural variables were averaged separately for neurons belonging to the mice in each group. Consistent with modulation by reward expectation, we found that cue-related activity was stronger and reward responses were weaker in the top-performing mice. Previous reward (which does not provide useful information for task performance) was more strongly represented in the bottom-performing mice (two-sided Wilcoxon signed-rank test, $n_1 = 129$ neurons in the top-performing mice, $n_2 = 104$ in the bottom-performing mice, with Holm–Bonferroni correction for the six tests). **f**, To investigate the relationship between instantaneous performance and neural encoding, for each session, all trials were grouped into blocks of ten consecutive trials with no overlap; these blocks were split into two groups based on whether the average performance in the block was greater or less than the median performance across all blocks in that session. The relative contributions of all behavioural variables calculated separately for the better- or worse-performance blocks are shown. The results did not show a significant difference for any of the variables (two-sided Wilcoxon signed-rank test, $n_1 = n_2 = 233$ neurons, with Holm–Bonferroni correction for the six tests).

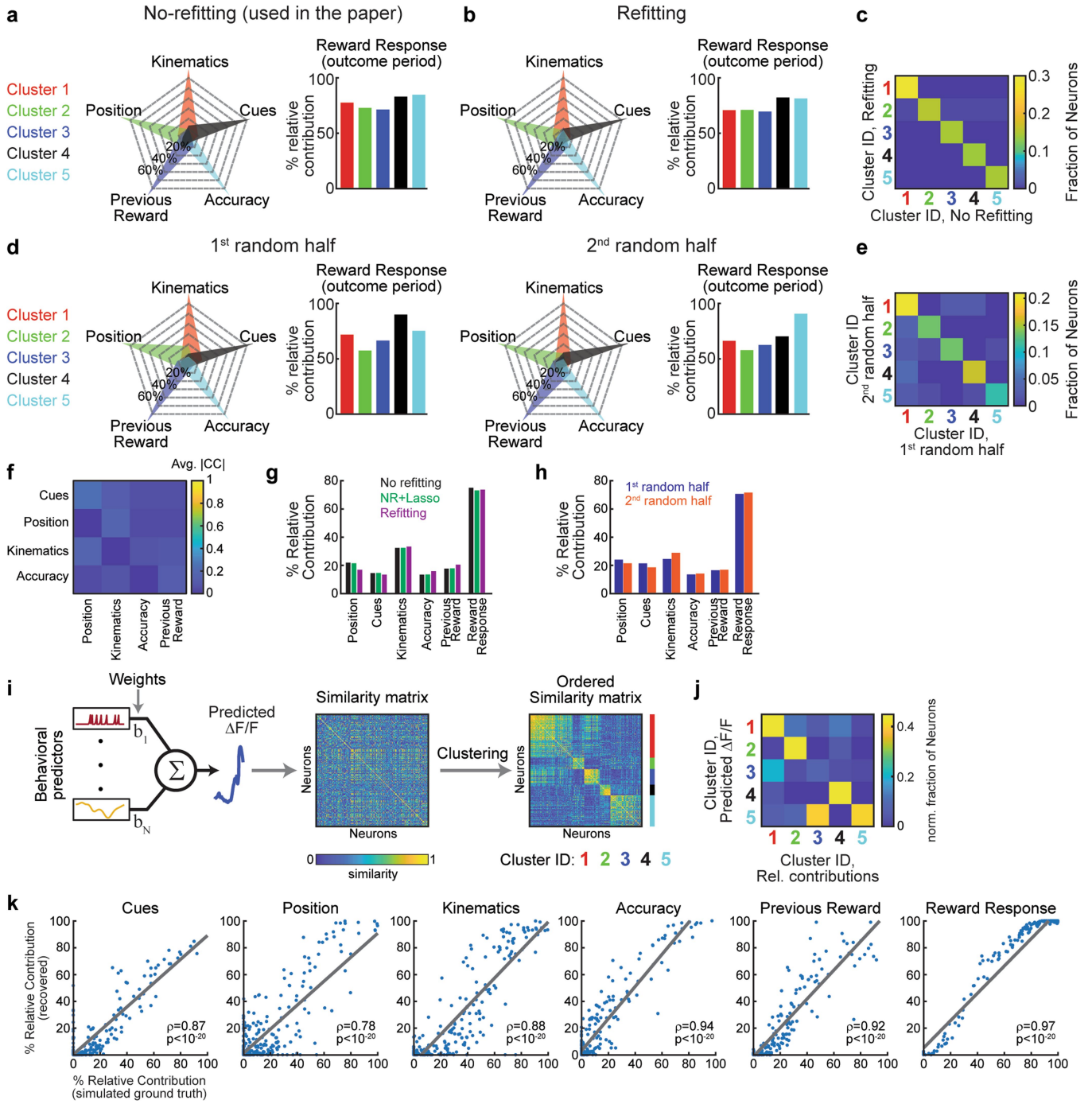

Extended Data Fig. 7 | See next page for caption.

Extended Data Fig. 7 | Validation of the clustering procedure and encoding model. a, Summary of average relative contributions of the different behavioural variables for neurons belonging to each cluster as calculated by the no-refitting approach (see Methods). Left, average relative contributions of cue period behavioural variables to neural activity for each cluster. Right, average relative contribution of reward for each cluster. **b**, As in **a**, but for the clustering analysis performed on the contributions calculated using the refitting approach (see Methods). **c**, Normalized confusion matrix for the cluster identities of each neuron, obtained by comparing the clustering of the relative contributions based on either the no-refitting or the refitting approach (see Methods for description of two approaches). The main diagonal represents neurons for which the cluster identities matched (97.8%). **d**, Average relative contributions of clusters obtained by separately analysing two random halves of the trials for each neuron. Correlations between the average relative contributions in each cluster across the two sets are as follows ($n = 5$ in all cases). Position: $\rho = 0.99$, $P < 8 \times 10^{-5}$. Cues: $\rho = 0.99$, $P < 4 \times 10^{-4}$. Kinematics: $\rho = 0.99$, $P < 2 \times 10^{-4}$. Accuracy: $\rho = 0.99$, $P < 3 \times 10^{-4}$. Previous reward: $\rho = 0.99$, $P < 0.001$. Reward response: $\rho = 0.48$, $P < 0.42$. **e**, Normalized confusion matrix for the cluster identities of each neuron, obtained by clustering the two random halves of the data. The main diagonal represents neurons for which the cluster identities matched (79.1%). Note that the chance level of matching is 20%. The matrix was calculated for neurons for which a cluster was assigned in the procedures for both halves of the data (>75% probability to belong to a cluster, $n = 91$). **f**, Average absolute value of the correlations for all pairs of predictors across all behavioural variables during the cue period (average across all predictor pairs and mice). **g**, Average relative contributions assessed separately using three different approaches: no refitting (NR; used in the paper); no refitting + Lasso regularization (NR + L); and refitting (R). Correlations between the results of the different approaches are as follows: ρ(NR, NR + L) = 1, $P < 7 \times 10^{-9}$. ρ(NR, R) = 0.99, $P < 1 \times 10^{-4}$. ρ(NR + L, R) = 0.99, $P < 8 \times 10^{-5}$ ($n = 6$ in all cases). When omitting the reward response contributions: ρ(NR, NR + L) = 1, $P < 2 \times 10^{-5}$. ρ(NR, R) = 0.91, $P < 0.04$. ρ(NR + L, R) = 0.92, $P < 0.03$ ($n = 5$ in all cases). Lasso regularization was applied using the lasso function in MATLAB; the mean square error (MSE) of the model was estimated using fivefold cross-validation, and we chose the lambda value that minimized the MSE. The results with lasso regularization were almost identical to the result without regularization, which suggests that there was not significant overfitting in our model. **h**, Average relative contributions assessed separately using two random halves of the data. For each neuron, we randomly divided all the trials in which the neuron was recorded into two separate subsets while matching the number of rewarded and previously rewarded trials between the subsets. Each subset of trials was then used to calculate the relative contributions of the behavioural variables ($\rho = 0.99$, $P < 3 \times 10^{-4}$ for all behavioural variables ($n = 6$), $\rho = 0.8$, $P < 0.11$ when omitting the reward response contributions ($n = 5$)). **i**, We tested the robustness of the clustering results by performing an alternative clustering procedure based on the predicted neuronal traces. After determining the regression weights for all neurons, behavioural predictors from one session were used to generate predicted activity traces for all neurons. A similarity matrix was constructed by taking the absolute correlation between the predicted traces for each neuronal pair. The similarity matrix was clustered using information-based clustering[20] (see Methods) and ordered by the obtained clusters (right panel; cluster identity for each neuron depicted by a coloured stripe to the right). **j**, Normalized confusion matrix for the cluster identities of each neuron, comparing clustering of the relative contributions (method used in the main text; Fig. 3) and the alternative method described here. The two clustering methods involve conceptual differences that may result in different clustering organizations. For example, the method used in Fig. 3, which clusters the relative contributions of the behavioural variables, is independent of a particular tuning for these variables, whereas the method presented here should be affected by such tuning (for example, upward versus downward position ramps). Nevertheless, we find a similar overall clustering structure between the two methods, with the main differences as follows. Original clusters 3 and 5 (associated with previous reward and accuracy) are joined in a single cluster (new cluster 5); and original cluster 1 (associated with kinematics) is now split into two clusters (new clusters 1 and 3). Further investigation of the split of the kinematics cluster showed that the neurons that split from the main kinematics cluster have stronger modulation for the view angle component of kinematics (based on the regression coefficient values). Such a split could not occur in the formulation used in the main text, which combined all the kinematics components (speed, acceleration and view angle). **k**, Further validation of the encoding model by simulating data with known relative contributions of the different behavioural variables. We replaced the activity of each neuron by a simulated trace that was computed using known relative contributions of the different behavioural variables as follows: first, the predictors corresponding to each behavioural variable were summed, resulting in one predictor per variable. Each predictor was z-scored and multiplied by a different relative contribution (taken from the values obtained for the real data). The scaled predictors were then summed, resulting in a single vector that forms the basis of the firing rate of the simulated neuron. To this vector, we added a constant to obtain an average firing rate close to 5 Hz (which was observed in in vivo electrophysiological recordings[22]). After zeroing negative values of this firing rate vector, we used it to generate a spike train using a Poisson process. Finally, the spike train was convolved with an approximate GCaMP kernel (see Methods). We proceeded to estimate the relative contributions for the simulated trace using the encoding model procedure. The relative contributions used to simulate the traces (x axis) and the recovered contributions (y axis) for a given behavioural variable are shown; the correlation between the original and recovered relative contributions and its associated P value are denoted ($n = 233$ in all cases).

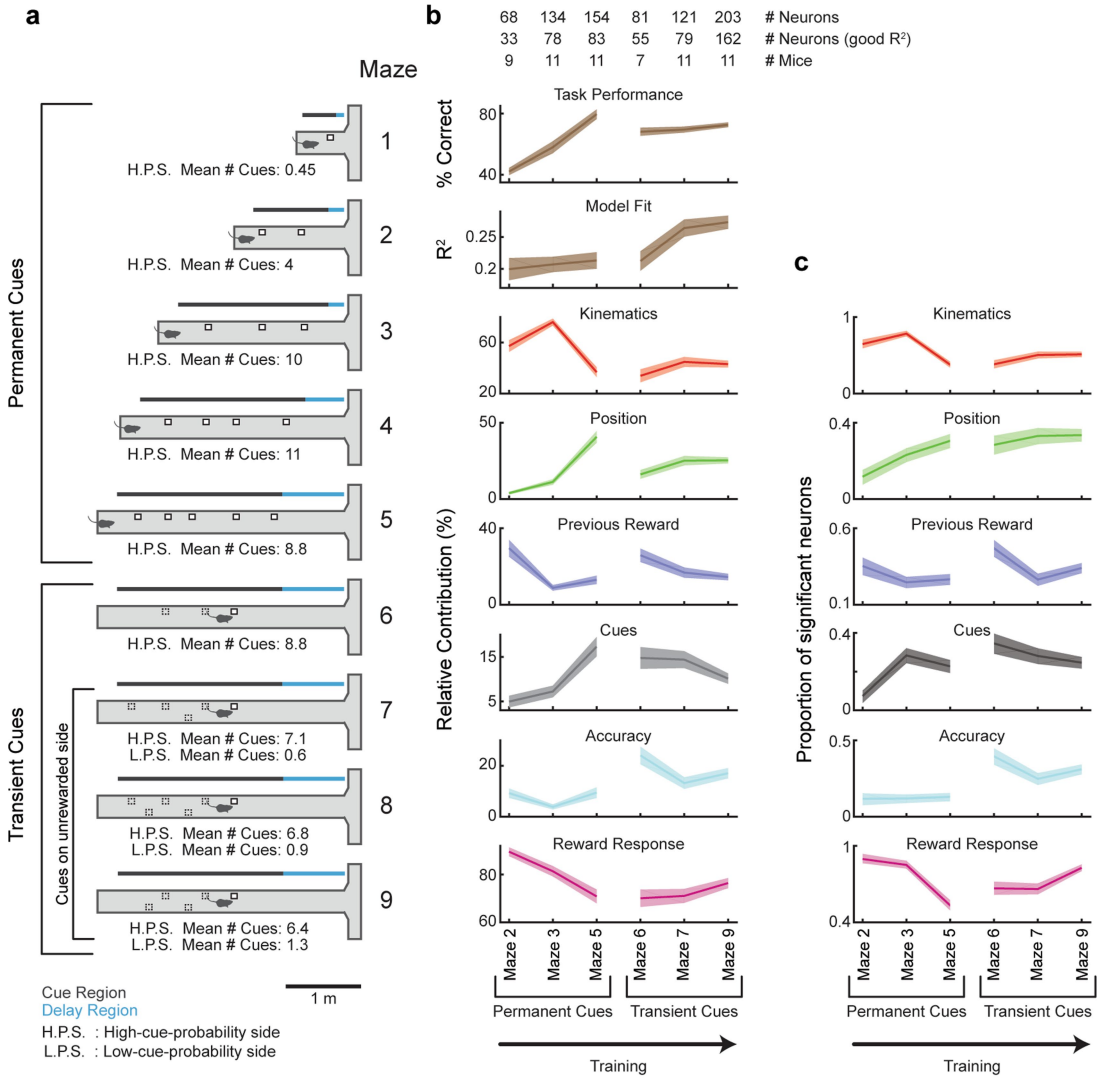

d

Maze #	1	2	3	4	5	6	7	8	9
Start region length (cm)	5	30	30	30	30	30	30	30	30
Cue region length (cm)	45	100	200	220	220	220	220	220	220
Delay region length (cm)	10	20	20	50	80	80	80	80	80
Permanent cues (y/n)	y	y	y	y	y	n	n	n	n
High-cue-probability side Poisson mean	0.45	4	10	11	8.8	8.8	7.1	6.8	6.4
Low-cue-probability side Poisson mean	none	none	none	none	none	none	0.6	0.9	1.3
Minimum performance for advancing (%)	0	60	80	80	80	80	75	75	-
Number of trials to calculate performance (for advancing)	20	80	100	100	100	100	100	100	-
Minimum number of sessions for advancing	0	0	1	1	2	2	2	1	-

Extended Data Fig. 8 | See next page for caption.

Extended Data Fig. 8 | Evolution of neural responses throughout learning. a, Schematic of the shaping protocol. Training consisted of nine mazes with increasing task difficulty. In the first five mazes, cues were permanent and were visible from the beginning of the trial (but still became progressively bigger as the mouse approached them). From maze 6 onward, cues only appeared when the mouse approached within 10 cm of their location. From maze 7 onward, cues could also appear on the unrewarded side. Cues were randomly distributed along the cue region. The number of cues on each side was sampled from a Poisson distribution with the mean indicated for each maze. **b**, Task performance, model fit and relative contributions of the behavioural variables throughout learning. The total number of neurons, the number of neurons with good model fit during the cue period ($R^2 > 5\%$; these were used to calculate the relative contributions of the behavioural variables during the cue period), and the number of mice analysed in each training stage are indicated at the top. Shaded colours are s.e.m. The results show that task performance increased steadily across the permanent cue mazes, and then dropped in the first transient cue maze, probably owing to the working memory component that is added in the transient cue mazes. The overall R^2 value of the behavioural model increased across learning, indicating that over the course of training, neural activity could be better explained by the measured behavioural variables. Notably, the relative contribution of position increased monotonically during the permanent cue mazes, but then dropped during the transient cue mazes, similar to the performance of the mice across the mazes. This is consistent with the interpretation of positional ramps as reflecting a value signal[3,18], because the expected value at each position is closely related to reward expectation for that session, and reward expectation is determined by average task performance. The relative contributions for cues also increased during early learning, consistent with being a reflection of the strength of the cue-reward association. Note that this value is decreased in the last maze, in which (because of the increased task difficulty) each cue has a lower predictive power with respect to reward. The relative contribution of previous reward decreased across the permanent cue mazes, then transiently increased during the first transient cue session. Because relying on previous reward is the wrong strategy in this task, this decrease in the relative contribution of previous reward may relate to mice weighting previous reward more heavily during the major steps in training when they have not yet learned the correct strategy for solving the task. The relative contribution of kinematics declined over the training procedure. This may be due to the kinematic aspect of the behaviour becoming less variable over training, as the mouse's motor skills improved for virtual-reality navigation. The relative contribution of trial accuracy was significantly higher during the transient cue mazes than the permanent cue mazes. This result potentially suggests that DA activity is correlated with task performance preferentially when there is a working memory component. The reward response declined during the permanent cue mazes, and remained relatively consistent during the transient cue mazes; this is consistent with an RPE signal, as RPE indicates negative modulation of reward responses by reward expectation (and reward expectation is related to task performance). **c**, Proportion of neurons that were significantly modulated by the different behavioural variables throughout learning (see Methods). Shaded colours show the 1 s.d. confidence intervals for a binomial distribution calculated using Jeffreys method. **d**, Details of the shaping procedure. The table lists the parameters of the mazes progressively used during the shaping of the behaviour. The 'permanent cues' field indicates whether the cues were presented at the beginning of the trial; otherwise, each cue was presented when the mouse was 10 cm away from its location. 'High- (and low) -cue-probability side mean' indicates the means of the Poisson distribution from which the number of cues presented on each side were drawn (at least one cue was always drawn); 'none' indicates that no cues were presented for the low-probability side on any trial in that maze. The mice were automatically advanced to the next maze if the following criteria were met: (1) their performance was above a predetermined threshold ('minimum performance for advancing' field) for a given number of trials ('number of trials to calculate performance' field). (2) They completed at least n sessions in the current maze, in which n is given by the 'minimum number of sessions for advancing' field.

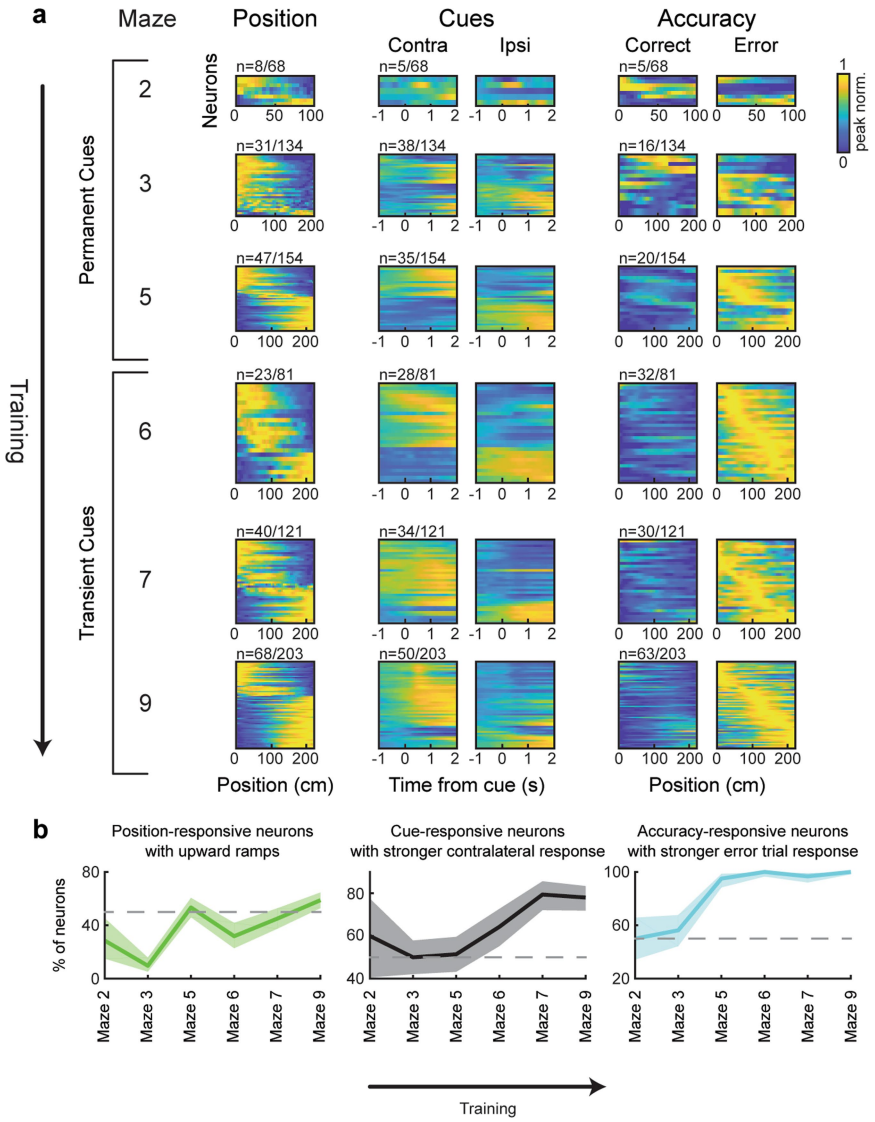

Extended Data Fig. 9 | Neural responses related to position, cues and accuracy throughout learning. a, For each behavioural variable (position, cues and accuracy), each heat map contains all significant neurons for that maze, with each row representing the average response of one neuron (the activity of each neuron is normalized by its peak). Statistical significance is assessed by comparing the *F*-statistic obtained from a nested model comparison with or without each behavioural variable to a distribution of the same *F*-statistic obtained from shuffled data (see Methods). In the case of position and accuracy, the averaging is over trials. In the case of cues, the averaging is across cue occurrences, and the average baseline activity was subtracted (in the second preceding the cue occurrence). The numbers of significant and total neurons for that variable and maze are indicated at the top of each heat map. The height of the heat maps for each maze is proportional to the average fraction of significant neurons (across variables) for that maze. **b**, Changes in tuning across learning. Left, percentage of neurons with significant responses to position that exhibited a positive slope in their average response. Middle, percentage of neurons with significant responses to cues that exhibited higher response to contralateral cues (compared to ipsilateral cues). Right, percentage of neurons with significant responses to accuracy that exhibited higher response in error trials (compared to correct trials). Shaded colours show the 1 s.d. confidence intervals for a binomial distribution calculated using Jeffreys method. The horizontal dotted lines indicate 50% in each panel. Position-selective neurons exhibited early in training more downward ramps than upward ramps (left, mazes 2 and 3). Because upward, and not downward, ramps are consistent with a value signal[3,18], this result suggests an evolution in the specific tuning—and not only the strength of representation—of this variable that is consistent with a value signal. Throughout training, cue-selective neurons are mostly selective for either contralateral or ipsilateral cues, and the preferential representation of contralateral cues develops late in training. This is interesting, because selectivity for contralateral versus ipsilateral cues is not a prediction of the RPE framework. Accuracy-selective neurons exhibit a strong bias towards elevated activity for error trials versus correct trials, which was evident by the last permanent cue maze.

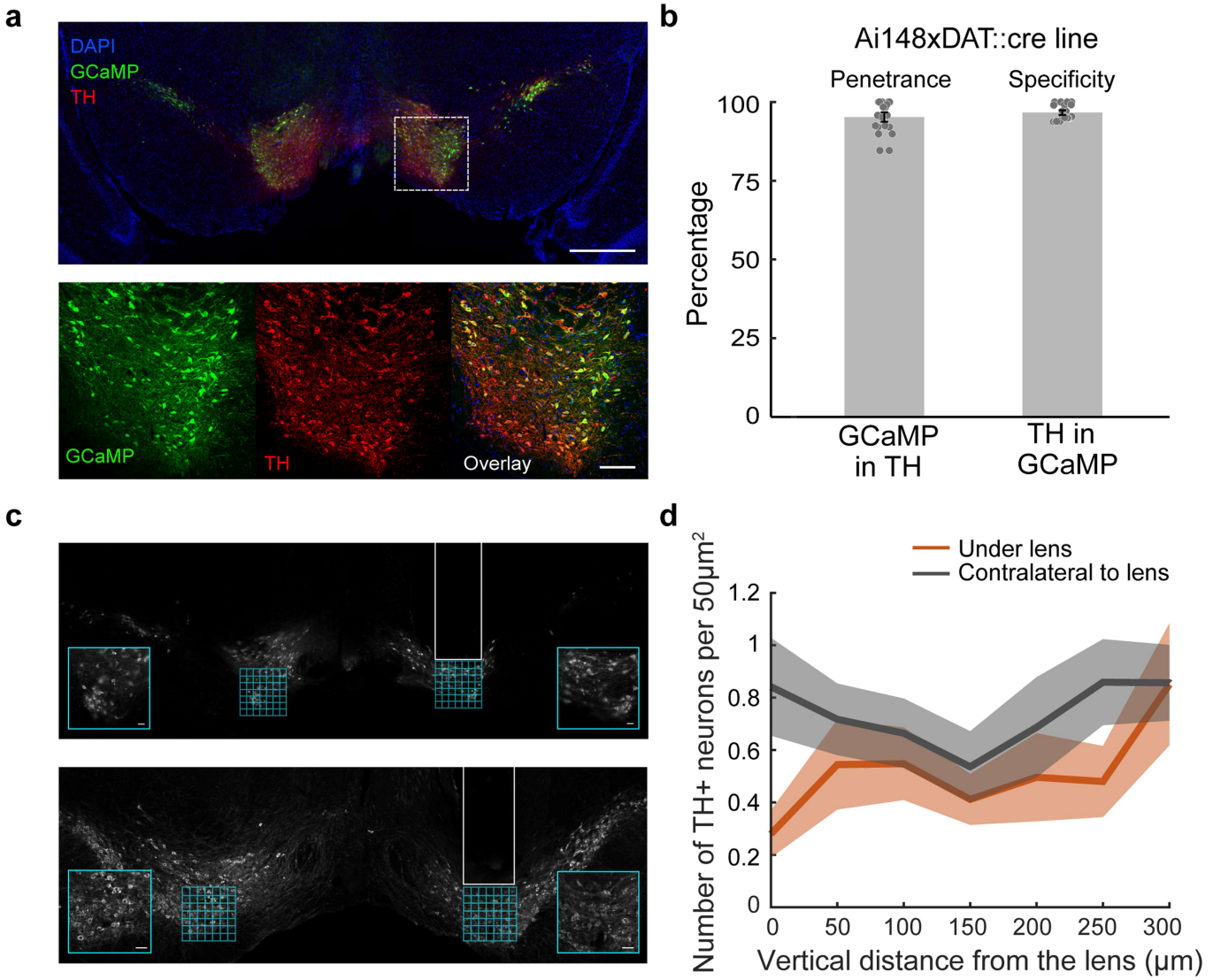

Extended Data Fig. 10 | Specific expression of GCaMP6f in midbrain dopamine neurons in the Ai148×DAT::cre mouse line. a, Example GCaMP6f expression (green) and tyrosine hydroxylase (TH) antibody staining (red). Square indicates location of high-magnification view of GCaMP expression in TH^+ neurons. Scale bars, 500 μm (top) and 100 μm (bottom). **b**, Quantification of penetrance and specificity of the Ai148×DAT::cre mouse line. Penetrance is the number of TH^+ neurons also expressing GCaMP (mean: 95.2%; s.e.m.: 1.52%; $n = 11$ sections; 1,082 cells, 2 mice). Specificity is the number of $GCaMP^+$ neurons that are also TH^+ (mean: 96.7%; s.e.m.: 0.74%; $n = 11$ sections; 1,075 cells, 2 mice). **c**, Examples of lesions caused by GRIN lens implants (left). Insets are higher-magnification images of the regions in which TH^+ neurons were counted underneath the lens and compared to counts contralateral to the lens. Scale bars, 50 μm. White overlay indicates location of the lesion. Cells were counted in 50 μm by 50 μm squares from 0–300 μm below the lens. **d**, Average number of TH^+ neurons per 50 μm^2 by distance from the bottom of the lens. Orange denotes average count under the lens; grey denotes average count from the contralateral hemisphere. Shading denotes s.e.m. $n = 11$ mice.

nature research

Corresponding author(s): Ilana Witten

Reporting Summary

Nature Research wishes to improve the reproducibility of the work that we publish. This form provides structure for consistency and transparency in reporting. For further information on Nature Research policies, see Authors & Referees and the Editorial Policy Checklist.

Statistical parameters

When statistical analyses are reported, confirm that the following items are present in the relevant location (e.g. figure legend, table legend, main text, or Methods section).

n/a	Confirmed	
☐	☒	The exact sample size (*n*) for each experimental group/condition, given as a discrete number and unit of measurement
☐	☒	An indication of whether measurements were taken from distinct samples or whether the same sample was measured repeatedly
☐	☒	The statistical test(s) used AND whether they are one- or two-sided *Only common tests should be described solely by name; describe more complex techniques in the Methods section.*
☐	☒	A description of all covariates tested
☐	☒	A description of any assumptions or corrections, such as tests of normality and adjustment for multiple comparisons
☐	☒	A full description of the statistics including central tendency (e.g. means) or other basic estimates (e.g. regression coefficient) AND variation (e.g. standard deviation) or associated estimates of uncertainty (e.g. confidence intervals)
☐	☒	For null hypothesis testing, the test statistic (e.g. *F*, *t*, *r*) with confidence intervals, effect sizes, degrees of freedom and *P* value noted *Give P values as exact values whenever suitable.*
☒	☐	For Bayesian analysis, information on the choice of priors and Markov chain Monte Carlo settings
☒	☐	For hierarchical and complex designs, identification of the appropriate level for tests and full reporting of outcomes
☐	☒	Estimates of effect sizes (e.g. Cohen's *d*, Pearson's *r*), indicating how they were calculated
☐	☒	Clearly defined error bars *State explicitly what error bars represent (e.g. SD, SE, CI)*

Our web collection on statistics for biologists may be useful.

Software and code

Policy information about availability of computer code

Data collection	Imaging data was collected using ScanImage 2015. Behavioral data was collected using Matlab code (Matlab 2015b, Mathworks Inc) based on the ViRMEn package (https://pni.princeton.edu/pni-software-tools/virmen-virtual-reality-matlab-engine).
Data analysis	Most of the analyses were done using custom Matlab code (Matlab 2017a, Mathworks Inc). optimized rigid motion-correction was done using python (anaconda python 2.7) and the OpenCV package (3.0). Multinomial mixed effects regression was done using stata (Stata/SE 14.2 for Unix).

For manuscripts utilizing custom algorithms or software that are central to the research but not yet described in published literature, software must be made available to editors/reviewers upon request. We strongly encourage code deposition in a community repository (e.g. GitHub). See the Nature Research guidelines for submitting code & software for further information.

Data

Policy information about availability of data

All manuscripts must include a data availability statement. This statement should provide the following information, where applicable:

- Accession codes, unique identifiers, or web links for publicly available datasets
- A list of figures that have associated raw data
- A description of any restrictions on data availability

The data that support the findings of this study are available from the corresponding author upon reasonable request

Field-specific reporting

Please select the best fit for your research. If you are not sure, read the appropriate sections before making your selection.

☒ Life sciences ☐ Behavioural & social sciences ☐ Ecological, evolutionary & environmental sciences

For a reference copy of the document with all sections, see nature.com/authors/policies/ReportingSummary-flat.pdf

Life sciences study design

All studies must disclose on these points even when the disclosure is negative.

Sample size	Statistical calculations were not used to choose the sample size. Number of animals and neurons were chosen to establish a comprehensive database of recordings of genetically identified dopamine neurons. to our knowledge, the number of recorded neurons (303) is the largest ever reported number of identified dopamine neurons in a single study.
Data exclusions	Neurons were excluded from the study using pre-established criteria. Neurons were selected for analysis based on visual inspection of recording stability, using both the images as well as ΔF/F traces. Only neurons that were stable for at least 50 trials were included in the dataset.
Replication	Statistical methods were used to ensure that the neuronal findings were not due to inter-mice variability.
Randomization	There was only one experimental group, thus no randomization was needed.
Blinding	There was only one group thus no group allocation blinding was necessary.

Reporting for specific materials, systems and methods

Materials & experimental systems

n/a	Involved in the study
☒	☐ Unique biological materials
☐	☒ Antibodies
☒	☐ Eukaryotic cell lines
☒	☐ Palaeontology
☐	☒ Animals and other organisms
☒	☐ Human research participants

Methods

n/a	Involved in the study
☒	☐ ChIP-seq
☒	☐ Flow cytometry
☒	☐ MRI-based neuroimaging

Antibodies

Antibodies used	Primary: TH Antibody: Aves labs, E.C. 1.14.16.2, chicken polyclonal anti-peptide antibody mixture. Catalog #: TYH. Lot #: TYH88967984. GFP antibody: Molecular probes, rabbit monoclonal. Catalog #: G10362. Lot #: 1787904. Secondary: Alexa fluor 647, Jackson ImmunoResearch Donkey-anti-chicken, Catalog #: 703-605-155. Lot #: 128273. Alexa fluor 488, Jackson ImmunoResearch, Donkey anti-rabbit, Catalog #: 711-545-152. Lot #: 130816.
Validation	TH: from manufacturer: "Quality Control: Both of the anti-peptide antibodies were analyzed by immunohistochemistry (at a concentration of 3 ug/ml) using fluorescein-labeled goat anti-chicken IgY (1:500 dilution, Aves Labs Cat.#F-1005) as the secondary reagent." This antibody was used in many previous works, including:

Carter et al. "Tuning arousal with optogenetic modulation of locus coeruleus neurons" Nature Neuroscience volume 13, pages 1526–1533 (2010).
Parker et al. "Reward and choice encoding in terminals of midbrain dopamine neurons depends on striatal target" Nature Neuroscience volume 19, pages 845–854 (2016)
GFP: from manufacturer: "All anti-GFP antibody conjugates are suited for detection of native GFP, GFP variants, and most GFP fusion proteins by western blot analysis and immunocytochemistry. The anti-GFP rabbit polyclonal antibody is raised against GFP isolated directly from Aequorea victoria and the IgG fraction is purified by ion-exchange chromatography." This antibody was used in many previous works, including:
Viswanathan et al. "High-performance probes for light and electron microscopy" Nature Methods volume 12, pages 568-576 (2015)
Zhang et al. "HACE1-dependent protein degradation provides cardiac protection in response to haemodynamic stress" Nature Communications volume 5, (2014) 10.1038/ncomms4430

Animals and other organisms

Policy information about studies involving animals; ARRIVE guidelines recommended for reporting animal research

Laboratory animals	2 strains of mice were used: either male DAT::IRES-Cre mice (n=14, The Jackson Laboratory strain 006660) or male mice resulting from the cross of DAT::IREScre mice and the GCaMP6f reporter line Ai148 mice (n=17, Ai148xDAT::cre, The Jackson Laboratory strain 030328). All mice were 2-6 months old during their use in the study.
Wild animals	the study did not involve wild animals
Field-collected samples	the study did not involve samples collected from the field